

September 27, 2018

MASTER THESIS

Optical Nonlinearity in Titanium Dioxide Waveguides

E.J.P. Vissers

**Faculty of Electrical Engineering, Mathematics and Computer Science
Optical Sciences**

Exam committee:

S.M. Martinussen M.Sc.

Dr. S.M. García Blanco

Dr. ir. D.A.I. Marpaung

UNIVERSITY OF TWENTE.

Abstract

Due to its high linear- and nonlinear refractive index, titanium dioxide is a promising material for utilizing nonlinear effects in waveguides. The transparency of titanium dioxide for visible light opens possibilities to use these nonlinear effects in the visible range of the spectrum. Using simulations, waveguide designs with minimal dispersion at wavelengths of 1310 nm and 1550 nm are proposed. A fabrication process is developed that allows fabrication of TiO₂ on SiO₂ waveguides with a sidewall angle between 76° and 86°, with a maximum thickness of 400 nm. TiO₂ waveguides with thicknesses of 74 nm and 360 nm have been fabricated, and their propagation losses have been measured using a camera. At a wavelength of 785 nm, the 74 nm thick waveguide has propagation losses of 8.2 dB/cm. The best propagation loss of the 360 nm thick waveguides at 785 nm was measured to be 13.4 dB/cm, while at a wavelength of 1310 nm, the losses are 2.20 ± 0.25 dB/cm. It has been found the waveguides with a thickness of 360 nm contain polycrystalline anatase TiO₂, while the waveguides with a thickness of 74 nm were of completely amorphous TiO₂. Four wave mixing experiments to verify the nonlinear refractive index at a wavelength of 1300 nm were not successful in the proposed waveguide with low dispersion at 1310 nm. This was because the available laser power was not high enough. A measurement setup for measuring four wave mixing at 980 nm wavelengths is proposed.

Contents

List of Figures	iv
List of Tables	vi
1 Introduction	1
1.1 The use of photonic integrated circuits	1
1.2 Nonlinear optics	1
1.3 Reasons for utilizing TiO ₂ as nonlinear optical material	2
1.4 Outline of thesis	3
2 Theory	4
2.1 Waveguide propagation loss mechanisms	4
2.2 Nonlinear optics theory	5
3 Waveguide design for four wave mixing	10
3.1 TiO ₂ FWM waveguide design	10
4 Waveguide fabrication	14
4.1 Sputtering titanium dioxide layer	14
4.2 Etching of titanium dioxide	18
4.3 Summary and conclusions	29
5 Waveguide Characterization	30
5.1 Measurement methods	30
5.2 Initial waveguides characterization	32
5.3 Effects of deposition and etching time on morphology and propagation losses	41
5.4 Propagation loss reduction by modified sputtering process	43
5.5 Summary and conclusion	46
6 Nonlinear measurement	48
6.1 Four wave mixing measurement setup	48
6.2 Dispersion analysis of fabricated waveguides	49
6.3 FWM measurement at 1300 nm	50

6.4 FWM measurement at 980 nm	53
7 Summary and conclusions	55
7.1 Zero-dispersion waveguide fabrication	55
7.2 Waveguide propagation losses	55
7.3 FWM measurement	56
8 Outlook	57
8.1 TiO ₂ layer growth	57
8.2 Utilizing anomalous dispersion	58
Bibliography	59
A Process flow for waveguide fabrication	64
A.1 Wafer preparation	64
A.2 TiO sputtering	64
A.3 Photolithography	65
A.4 Etching	67
B Determining propagation losses from images using Matlab	68
B.1 Matlab code	68
C XPS measurements	71

List of Figures

3.1	Dispersion for differing waveguide widths and heights for 1000 nm light.	11
3.2	Dispersion for differing waveguide widths and heights for 2 wavelengths. The black line indicates points of no dispersion, the grey lines show the points of ± 100 ps/nm/km dispersion. The red line shows the crossover point between a single- and dual-mode waveguide.	12
4.1	Sputtering curve, showing the bias voltage (black circles) and deposition rate (blue squares) as a function of oxygen fraction in the gas flow	16
4.2	Photograph of a used sputtering target. A new target is completely flat.	16
4.3	Surface roughness images of two waveguides with differing thickness. .	18
4.4	Waveguide etched in [23] using initial settings in Table 4.2 for 15 minutes	21
4.5	Etch profile of 65 nm TiO_2 layers on 8 μm SiO_2 samples etched at 20 W using the settings in Table 4.3, with varying O_2 flows. In each image, the thin dark line on the cross section is the TiO_2 on top of SiO_2 . A platinum layer was deposited on top of the TiO_2 to prevent FIB rounding effects. .	24
4.6	Etch profile of 360 nm TiO_2 layers on 8 μm SiO_2 samples etched at 20 W using the settings in Table 4.3, with different O_2 flows and etching times. A platinum layer was deposited on top of the TiO_2 to prevent FIB rounding effects.	25
4.7	Resist and TiO_2 etch rates of the recipe in Table 4.3, using 20 W HF power, and 6 sccm O_2	27
4.8	Etch profile of 360 nm TiO_2 layers on 8 μm SiO_2 samples etched using the optimal etch settings for 5 minutes and 30 seconds. The mask width is varied in each picture	28
4.9	Etch rate along the diameter of the wafer.	29
5.1	Energy level diagram of Raman scattering. Modified from [25].	31
5.2	First order mode calculated for two 1.2 μm wide waveguides of differing thickness.	33
5.3	loss measurements of a 75 and 360 nm thick spiral waveguide.	34
5.4	Raman signal of two waveguides of different thickness. The peaks at 384 cm^{-1} and 643 cm^{-1} in the spectrum for the 360 nm thick waveguide indicate the presence of anatase TiO_2	35

5.5	Propagation losses around the C-band for 360 nm thick waveguide. . . .	36
5.6	FTIR measurement and reflectance simulation for the measured TiO ₂ layer.	38
5.7	Raw B-trace data, and the spline fit.	39
5.8	Raman spectra of 4 waveguides, with differing layer thickness and etch depths. Each spectrum has been offset for visibility.	42
5.9	Raman spectrum of three waveguides, one fabricated using the modified, split deposition process, and two using the unmodified process, using a single deposition.	44
5.10	Loss at several wavelengths for two waveguides of 360 nm thickness. One waveguide is from a TiO ₂ layers sputtered in one deposition run, while the other one had the deposition process split into 6 short depositions.	45
6.1	Measurement setup for measuring FWM.	48
6.2	The simulated dispersion curves for fabricated 360 nm thick waveguides of different widths.	50
6.3	Four wave mixing results at 1300 nm. The probe beam power in the waveguide is 6.3 μ W CW. The pump beam power in the waveguide is 19 μ W time averaged, or 4.8 mW peak.	52

List of Tables

1.1	Linear and nonlinear refractive index of several materials.	2
4.1	Quantitative results of AFM roughness measurements, after correcting for wafer tilt and bow.	17
4.2	Starting point etch settings, from [23]	20
4.3	Initial etch settings variations	22
4.4	Etch rates and selectivities of initial etch settings test on 65 nm TiO ₂ layers.	25
5.1	Raman spectrum peaks for rutile and anatase TiO ₂ , as measured by U. Balachandran and N. G. Error in [30]	32
5.2	Percentage of power in different areas for fundamental TE mode of two waveguides	33
5.3	Fabrication parameters and dimensions for four samples, used to com- pare the impact of the deposition and etching times on propagation losses of the resulting waveguides.	41
5.4	Propagation losses of 4 waveguide samples, for 633 and 785 nm light.	43

Chapter 1

Introduction

1.1 The use of photonic integrated circuits

Ever since the introduction of electronic integrated circuits, the performance of these chips has been increasing steadily. This was achieved by shrinking the transistor size, increasing their efficiency and/or switching speed. Communication channels, especially the internet, could not benefit from the downscaling, since these need to transmit over a certain length, thereby keeping their size up. This inability to scale leads to chips and systems that cannot get data to and from the outside world as fast as it can be processed. Replacing the electrical interconnects with optical fiber interconnects reduces this problem. Therefore, the first transatlantic fiber optic cable was installed in 1988 [1], with many more following after. The conversion between electrical and optical signalling is then achieved with optical transceivers on Photonic Integrated Circuits (PICs). This technology is already highly commercialized.

PICs have another application in the domain of (bio)sensing. Measurements can be done on both gasses and fluids in this way. Since the surface area of these chips is small, only a small amount of analyte, less than a millilitre is necessary to do the measurement [2]. When a blood analysis could be moved from a lab-based procedure to analysis on an optical chip, this would reduce the invasiveness of taking a blood sample from a patient.

1.2 Nonlinear optics

Nonlinear optics is a field that started in 1961 with a paper by P. A. Franken et al. [3]. It was the first paper where second harmonic generation was measured. The signal achieved in the measurement was so small it's pointed out by an arrow in the original paper, and the speck is not visible on modern scans of the paper. Despite this, it started a whole lot of research. Nonlinear effects are often a nuisance, since they potentially distort data signals in optical communication systems [4]. Nonlinear effects have however also been utilized for communication systems, by encoding data using

solitons [5]. Another useful application of nonlinear is in Optical Parametric Oscillators (OPOs), allowing a large range of wavelengths to be generated from a high power single wavelength source [6]. An OPO is utilized in this thesis as well.

1.3 Reasons for utilizing TiO₂ as nonlinear optical material

Virtually all modern electronics are fabricated using silicon, with other materials only being used for specialized applications. The materials used to fabricate PICs are more diverse.

Currently, three of the materials often used in commercial PICs are silicon nitride (Si₃N₄), Silicon (Si) and Indium Phosphide (InP). Silicon nitride is used for its low propagation losses (lower than 0.03 dB/cm has already been achieved) and large transparency window [7]. Silicon is used for its high linear refractive index ($n=3.44$ [8]) and high nonlinear Kerr refractive index ($n_2 = 4.4 \times 10^{-18} \text{ m}^2/\text{W}$ [9]). Indium Phosphide is used because it can be used as an electrically pumped optical gain medium.

TiO₂ might be a useful material for PICs as well, because of its linear and nonlinear refractive index, combined with its transparency window covering the visible range [10]. It has a similar nonlinear refractive index as Si₃N₄, but a higher linear refractive index. Through the higher confinement, this should lead to more efficient nonlinear devices from TiO₂ compared to Si₃N₄. Additionally, it has been shown TiO₂ can be doped with Erbium ions, which opens up the possibility of optical gain in the material [11]. The linear and nonlinear refractive index of the mentioned materials are given in Table 1.1. The data for Al₂O₃ and KYW are also given, since these are materials currently investigated and used in the Optical Sciences group.

Table 1.1: Linear and nonlinear refractive index of several materials.

Material	n	$n_2 \text{ m}^2/\text{W}$
TiO ₂	2.37 ^a	2.33E-19 [12]
Si ₃ N ₄	2.03 [13]	2.80E-19 [14]
Si	3.44 [8]	4.40E-18 [9]
InP	3.1 [15]	-
Al ₂ O ₃	1.76 [12]	4.02E-20[12]
KYW	2.1 [16]	2.40E-19 [16]

^a: Measured on our layers. -: No data found in literature.

The goal of this thesis is to investigate the possibility of using TiO₂ in PICs, especially for components exploiting the nonlinearity of the material. This will be done by developing a fabrication process that can be used to fabricate TiO₂ waveguides, and verifying whether the nonlinear refractive index of the material matches the value found in literature.

1.4 Outline of thesis

The thesis will continue with a chapter on the theory of waveguides and nonlinear optics. Chapter 3 is on the design of a TiO_2 waveguide that supports efficient four wave mixing. Using such a waveguide, the nonlinear refractive index of TiO_2 can be measured. Chapter 4 is about the fabrication processes used to fabricate waveguides. In chapter 5 the propagation losses and crystal structure of the waveguides are characterized. Chapter 6 is about the measurement of the nonlinear refractive index of TiO using the four wave mixing process. Chapter 7 will summarize the work done, and chapter 8 will provide future research that could still be done on the subject.

Chapter 2

Theory

This chapter will give some theory about waveguide propagation losses, and show the equations involved in Four Wave Mixing in waveguides.

2.1 Waveguide propagation loss mechanisms

In theory, waveguides made of transparent materials are lossless devices. Since the light is confined in two dimensions, all light that is coupled into a waveguide-mode will stay in that mode. However, fabricated devices are not lossless. The two mechanisms that always lead to propagation losses in fabricated waveguides are scattering and material-absorption [17]. For waveguide sections that make a turn, bending losses will also play a role [17].

2.1.1 Scattering losses

Scattering losses are caused by imperfections in the waveguide. If the imperfections are on a material boundary, these lead to surface scattering losses. If they reside within a single material, they lead to volume scattering losses.

Surface scattering

Surface scattering can be understood using the ray picture of light in a waveguide. For a perfectly smooth waveguide, once a ray is travelling in the waveguide, it'll be completely reflected each time it hits one of the waveguide surfaces, since the incident angle will stay constant. Once imperfections on the surface are introduced, the incident angle will be different for each interaction of the ray with the wall. If the incident angle drops below the critical angle for one of the interactions, part of the light will travel to the other side of the wall, and be radiated from the waveguide. It was measured in [18] that the scattering off the surface of a waveguide can be modelled as Mie scattering.

Volume scattering

Scattering can also take place inside the waveguide itself, due to microscopic refractive index differences throughout the layer. These scatter points will scatter light in random directions, therefore taking power out of the propagating mode, and radiating it in a different direction. These losses are usually low compared to the surface radiation [17].

2.1.2 Material absorption losses

Material losses are caused in a waveguide due to partial absorption of the waves by the materials that make up the waveguide. The absorption coefficient of a material is the imaginary part of the refractive index, often called k . These losses are not expected in TiO_2 on SiO_2 waveguides for the wavelengths in the visible in NIR range, since both TiO_2 and SiO_2 are transparent materials for that range [10].

2.1.3 Bending losses

When the waveguide is not straight, but is bended, part of the light will be radiated out of the outer wall of the waveguide. The effect becomes more severe with tighter bends, and also with lower index contrasts between the waveguide core and cladding.

2.2 Nonlinear optics theory

2.2.1 Nonlinear polarization

When light travels through a medium, the electric field of the light induces a polarization $\tilde{P}(t)$. For ordinary linear media, the induced polarization is $\tilde{P}(t) = \epsilon_0 \chi^{(1)} \tilde{E}(t)$, where ϵ_0 is the vacuum permittivity, $\chi^{(1)}$ is the linear susceptibility of the medium, and $\tilde{E}(t)$ is the electric field. The linear polarization field therefore contains only frequencies that are equal to those of the E-field that induced them.

For a nonlinear medium, the induced polarization is not only proportional to \tilde{E} , but also to all its integer powers as follows:

$$\tilde{P} = \epsilon_0 (\chi^{(1)} \tilde{E} + \chi^{(2)} \tilde{E}^2 + \chi^{(3)} \tilde{E}^3 + \dots) = \tilde{P}^{(1)} + \tilde{P}^{(2)} + \tilde{P}^{(3)} + \dots \quad (2.1)$$

In this expression, $\chi^{(i)}$ is the i th order optical susceptibility of the medium, and $\tilde{P}^{(i)}$ the i th order polarization.

When the nonlinear optical susceptibilities are taken into account, it becomes clear that the polarization can have frequency components that are not present in the electric field that induced them. The simplest nonlinear effect to show this mathematically is second harmonic generation: If the electric field contains a pure sine wave at radial frequency ω , like $\tilde{E} = A \sin(\omega t)$, the second order polarization becomes:

$$\tilde{P}^{(2)} = \epsilon_0 \chi^{(2)} A^2 \sin^2(\omega t) = \epsilon_0 \chi^{(2)} A^2 \left(\frac{1}{2} - \frac{\cos(2\omega t)}{2} \right) \quad (2.2)$$

In this case, the second order polarization will contain a DC component, and a component at a frequency of 2ω , the second harmonic of the original frequency.

2.2.2 Four Wave Mixing

The nonlinear process that's often used in literature to measure $\chi(3)$ in waveguide materials is Four Wave Mixing (FWM). This process takes place when two frequencies of light ω_1 and ω_2 are propagating through a medium with a non-zero third-order nonlinear susceptibility, leading to the following expressions:

$$\tilde{E} = Ae^{-i\omega_1 t} + Be^{-i\omega_2 t} + \text{c.c.} \quad (2.3)$$

$$\begin{aligned} \tilde{P}^{(3)} \propto \tilde{E}^3 = & A^3 e^{-3i\omega_1 t} \\ & + 3A^2 B e^{-2i\omega_1 t} e^{-i\omega_2 t} \\ & + 3AB^2 e^{-i\omega_1 t} e^{-2i\omega_2 t} \\ & + B^3 e^{-3i\omega_2 t} + \text{c.c.} \end{aligned} \quad (2.4)$$

In these formulas $A = A_0 e^{ik_1 z}$ and $B = B_0 e^{ik_2 z}$.

The frequency components present in each component of polarization are the following:

- $A^3 e^{-3i\omega_1 t} + \text{c.c.}$: ω_1 and $3\omega_1$
- $3A^2 B e^{-2i\omega_1 t} e^{-i\omega_2 t} + \text{c.c.}$: $2\omega_1 + \omega_2$, $2\omega_1 - \omega_2$ and ω_2
- $3AB^2 e^{-i\omega_1 t} e^{-2i\omega_2 t} + \text{c.c.}$: $2\omega_2 + \omega_1$, $2\omega_2 - \omega_1$ and ω_1
- $B^3 e^{-3i\omega_2 t} + \text{c.c.}$: ω_2 and $3\omega_2$

The frequencies that make up the four waves of FWM are in this case the four lowest frequencies: ω_1 and ω_2 being the initial frequencies, and $2\omega_1 - \omega_2$ and $2\omega_2 - \omega_1$ as the generated frequencies, which will be called ω_3 and ω_4 respectively.

The input frequencies ω_1 and ω_2 are often called the pump- and probe frequencies. If we take the generation of the frequency $\omega_3 = 2\omega_1 - \omega_2$ it can be seen that the polarization wave that contains the frequency is given by $3A^2 B e^{-2i\omega_1 t} e^{-i\omega_2 t} + \text{c.c.}$. This scales quadratically with A , the field with frequency ω_1 , and proportionally with B , the field with frequency ω_2 . In that case, ω_1 is called the pump frequency, while ω_2 is called the probe frequency. For the generation of ω_4 in the list above, the pump- and probe-frequencies are swapped, and ω_2 is the pump beam.

2.2.3 Phase matching

If we consider the generation of light at the frequency ω_3 by FWM, we already know it must have come from the polarization field $\tilde{P}^{(3)} \propto A_0^2 B_0 e^{-i((2k_1 - k_2)z - \omega_3 t)}$. The generated light will be described by $\tilde{E}_3 \propto e^{-i(k_3 z - \omega_3 t)}$, where k_3 is dependent on ω through the dispersion relation for the light in the waveguide.

The polarization field will induce an electric field with a fixed phase shift between the polarization and electric field at all distances along the polarization field at once [6]. Therefore, if the electric field's wavevector k_3 is different from the polarization field's wavevector $2k_2 - k_1$, the phase of the electric field generated from the polarization at $z = 0$ is different from the phase generated at other distances along the waveguide. The phase mismatch $\Delta\phi$ between the electric field and the polarization field built up after propagating a distance z is given by a spatial wave with the wavevector $\Delta k = 2k_1 - k_2 - k_3$ as follows:

$$\Delta\phi = e^{(i\Delta kz)} \quad (2.5)$$

Assuming the initial E-field is not depleted, which is correct for short interaction lengths and low generated e-field strengths, the total strength of the electric field in the generated wave \tilde{E}_{ω_3} after propagating for a distance z_p is then proportional to the integral of the phase mismatch over the propagation distance:

$$\tilde{E}_{\omega_3} \propto \int_0^{z_p} \cos(\Delta kz) dz = \frac{e^{(i\Delta kz_p)} - 1}{i\Delta k} \quad (2.6)$$

Or if the wavevector mismatch is 0:

$$\tilde{E}_{\omega_3} \propto \int_0^{z_p} dz = z_p \quad (2.7)$$

The maximum amount of electric field that can be generated is therefore inversely proportional to the wavevector mismatch. The propagation distance after which this strength is achieved is at the maximum of the sine-wave, so for $z = \frac{\pi}{2\Delta k}$, which is also called the coherence length [6].

2.2.4 FWM phase matching in waveguides

A parameter often used to evaluate the phase matching for FWM in a waveguide is the dispersion curve, which plots the dispersion D_λ in ps/nm/km as a function of wavelength. The expression for D_λ is the following [19]:

$$D_\lambda = -\frac{2\pi c}{\lambda^2} \frac{\partial^2 k}{\partial \omega^2} \quad (2.8)$$

If higher order derivatives than $\frac{\partial^2 k}{\partial \omega^2}$ are assumed to be zero, perfect phase matching for FWM is achieved if the center frequency (ω_1 in our example) is at the zero dispersion point. In that case, the function $k(\omega)$ becomes a linear function:

$$\frac{\partial^2 k}{\partial \omega^2} = 0 \quad (2.9)$$

$$\frac{\partial k}{\partial \omega} = c_1 \quad (2.10)$$

$$k(\omega) = c_1\omega + c_2 \quad (2.11)$$

The expression for the wavevector mismatch then becomes zero:

$$\Delta k = 2k(\omega_1) - k(\omega_2) - k(2\omega_1 - \omega_2) \quad (2.12)$$

$$\Delta k = c_1(2\omega_1 - \omega_2 - (2\omega_1 - \omega_2)) + 2c_2 - 2c_2 = 0 \quad (2.13)$$

The same principle can be used to calculate the wavevector mismatch for a certain pump and probe wavelength if the dispersion is non-zero:

$$\frac{\partial^2 k}{\partial \omega^2} = D_\omega = \frac{-D_\lambda \lambda^2}{2\pi c} \quad (2.14)$$

$$\frac{\partial k}{\partial \omega} = D_\omega \omega + c_1 \quad (2.15)$$

$$k(\omega) = \frac{1}{2} D_\omega \omega^2 + c_1 \omega + c_2 \quad (2.16)$$

The wavevector mismatch for four wave mixing then becomes:

$$\Delta k = -D_{\omega_1}(\omega_1 - \omega_2)^2 = \frac{D_{\lambda_1} \lambda_1^2}{2\pi c} \left(\frac{2\pi c}{\lambda_1} - \frac{2\pi c}{\lambda_2} \right)^2 \quad (2.17)$$

2.2.5 FWM conversion efficiency

The amount of power converted to a frequency ω_3 is not only dependent on the phase matching, but also linearly proportional to the strength of the polarization that induced it [6]. The polarization itself is proportional to $P_{\text{pump}}^2 P_{\text{probe}}$.

If loss is not taken into account, the strength of E field generated at frequency ω_3 after propagating for a distance z through the waveguide is given as:

$$E_{\omega_3} = \left(\frac{e^{(i\Delta k z_p)} - 1}{i\Delta k} \right) E_{\text{pump}}^2 E_{\text{probe}} \gamma \quad (2.18)$$

Or, assuming perfect phase matching:

$$E_{\omega_3} = L E_{\text{pump}}^2 E_{\text{probe}} \gamma \quad (2.19)$$

In these equations, L is the propagation length through the waveguide, and γ is a parameter that is dependent on the waveguide. All equations shown before were only one-dimensional. The parameter γ is the nonlinear parameter of the waveguide, which is given in the unit $\text{W}^{-1} \text{m}^{-1}$. It essentially represents an effective material, that describes the effective nonlinear properties of the waveguide as if it is described in one dimension. The equation for γ is as follows [20]:

$$\gamma = \frac{k_0 n_2}{A_{\text{eff}}} + i \frac{\beta_{\text{TPA}}}{2A_{\text{eff}}} \quad (2.20)$$

Where k_0 is the vacuum wavenumber of the light, n_2 the nonlinear Kerr refractive index, β_{TPA} the two photon absorption coefficient and A_{eff} = the effective mode area, defined as $\left(\int \int |E|^2 dx dy \right)^2 / \int \int |E|^4 dx dy$

the factor β_{TPA} in TiO_2 will be zero for all wavelengths above 813 nm, since only photons with a wavelength below 813 nm will contribute to TPA, due to the 3.05 eV bandgap of TiO_2 [21].

The measurement of the nonlinear parameter γ of a waveguide can therefore be used to measure the Kerr nonlinear refractive index n_2 .

In an actual measurement, the thing that can most easily be measured, and is independent of output-coupling efficiency, is the conversion efficiency CE , being the ratio between the generated-power P_{ω_3} , and the probe laser-power P_{ω_2} . This efficiency is given by the following equation, still assuming a lossless waveguide and perfect phase matching:

$$CE = \frac{P_{\omega_3}}{P_{\omega_2}} = \frac{E_{\omega_3}^2}{E_{\omega_2}^2} \quad (2.21)$$

$$CE = \frac{(LE_{\omega_1}^2 E_{\omega_2} \gamma)^2}{E_{\omega_2}^2} = (LP_{\omega_1} \gamma)^2 \quad (2.22)$$

Once losses are introduced, the length L is replaced with an effective length L_{eff} , which is given as $L_{\text{eff}} = \frac{1-e^{-\alpha L}}{\alpha}$ [22].

Chapter 3

Waveguide design for four wave mixing

As shown in the previous chapter, the dispersion characteristic of the waveguide dictates the propagation length over which FWM can occur. Therefore, a TiO₂ waveguide was designed to have low dispersion at the wavelengths where FWM could possibly be measured.

3.1 TiO₂ FWM waveguide design

Simulation setup

To find waveguides suitable for the FWM experiments, an eigenmode solver in Lumerical Mode was used to simulate the dispersion and number of modes of several TiO₂ channel waveguides. The starting point used was the waveguide used at 1550 nm by Guan et al. in [22]. This is a TiO₂ on SiO₂ channel waveguide with an etch angle of 70°, a thickness of 380 nm and a bottom width of 1150 nm.

The simulated waveguides were adjusted in several ways. Firstly, the TiO₂ refractive index was changed to the values measured on TiO₂ layers fabricated in our own cleanroom by I. Hegeman [23]. He had measured the refractive index using ellipsometry. The data was then fit to the Cauchy equation with three coefficients, giving the following expression for refractive index: $n(\lambda) = A + \frac{B}{\lambda^2} + \frac{C}{\lambda^4}$, where λ is the vacuum wavelength of light. The values for A , B and C were 2.212, 0.06283 and -0.00216 respectively, which were the average coefficients measured at 10 points on a single wafer.

For the initial simulations, thicknesses between 300 nm and 460 nm were simulated, to have 80 nm extra on both sides compared to the waveguide used in [22].

Since the photolithography masks available had a smallest waveguide of 0.8 μm wide, the widths simulated were set between 0.7 μm and 1.2 μm . If the etch process has some etch bias, 0.7 μm width might be achieved with the 0.8 μm masks.

To increase the dispersion for the waveguides, a slight overetch of 75 nm was used in the simulation as well, where the SiO₂ bottom cladding is etched 75 nm deep after

etching all the TiO_2 outside of the resist mask.

Simulation results

The dispersion for different waveguide dimensions was simulated for three different wavelengths: 1000, 1310 and 1550 nm. The 1000 nm wavelength was chosen since a Ti:Sapphire laser could be used as a high power pump at this wavelength. The 1310 nm and 1550 nm wavelengths were chosen because these are widely used for telecommunication applications. The simulation results can be seen in Fig. 3.1 and Fig. 3.2. The colour in the figures gives the simulated dispersion for each simulation, while the red lines in Fig. 3.2 show the dimensions where the waveguide transitions from supporting one to supporting two TE modes.

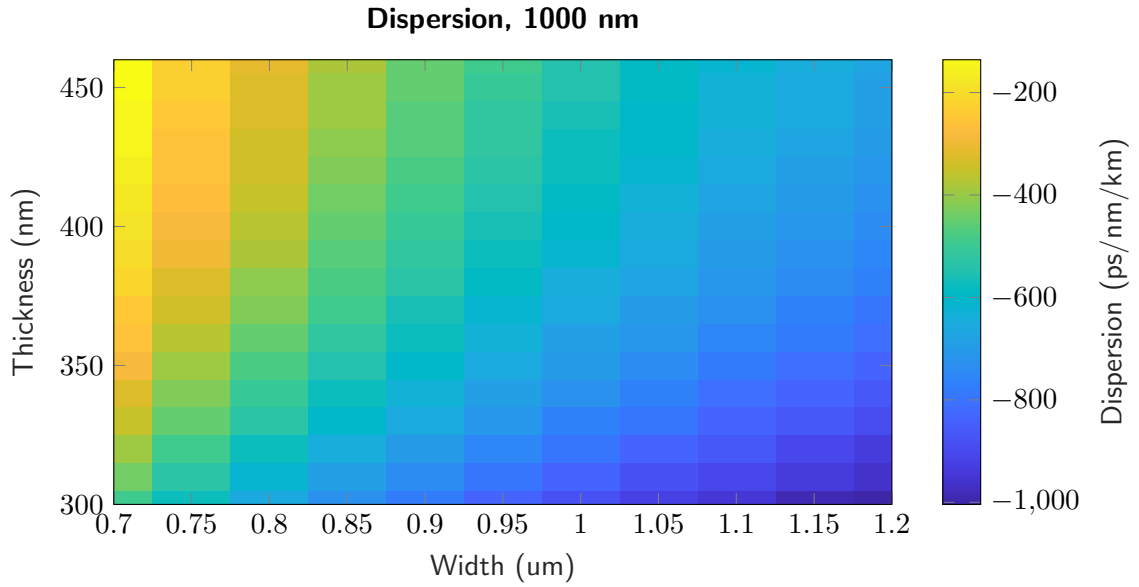


Figure 3.1: Dispersion for differing waveguide widths and heights for 1000 nm light.

From the simulated dispersion for 1000 nm light in Fig. 3.1 it can be seen that none of the simulated waveguide dimensions gives dispersions within ± 100 ps/nm/km. Therefore, it was decided to focus the rest of the work on waveguides with zero-dispersion near wavelengths of 1310 nm or 1550 nm.

3.1.1 Chosen waveguide dimensions for FWM measurement

Waveguides with no dispersion at 1310 nm or 1550 nm are likely within the fabrication possibilities with the available technology. Between these two wavelengths it was chosen to measure at a wavelength of 1310 nm for two reasons: Firstly, no publications could be found where FWM in TiO_2 waveguides was measured at this wavelength. Secondly, the required TiO_2 layer thickness is lower for a wavelength of 1310 nm compared

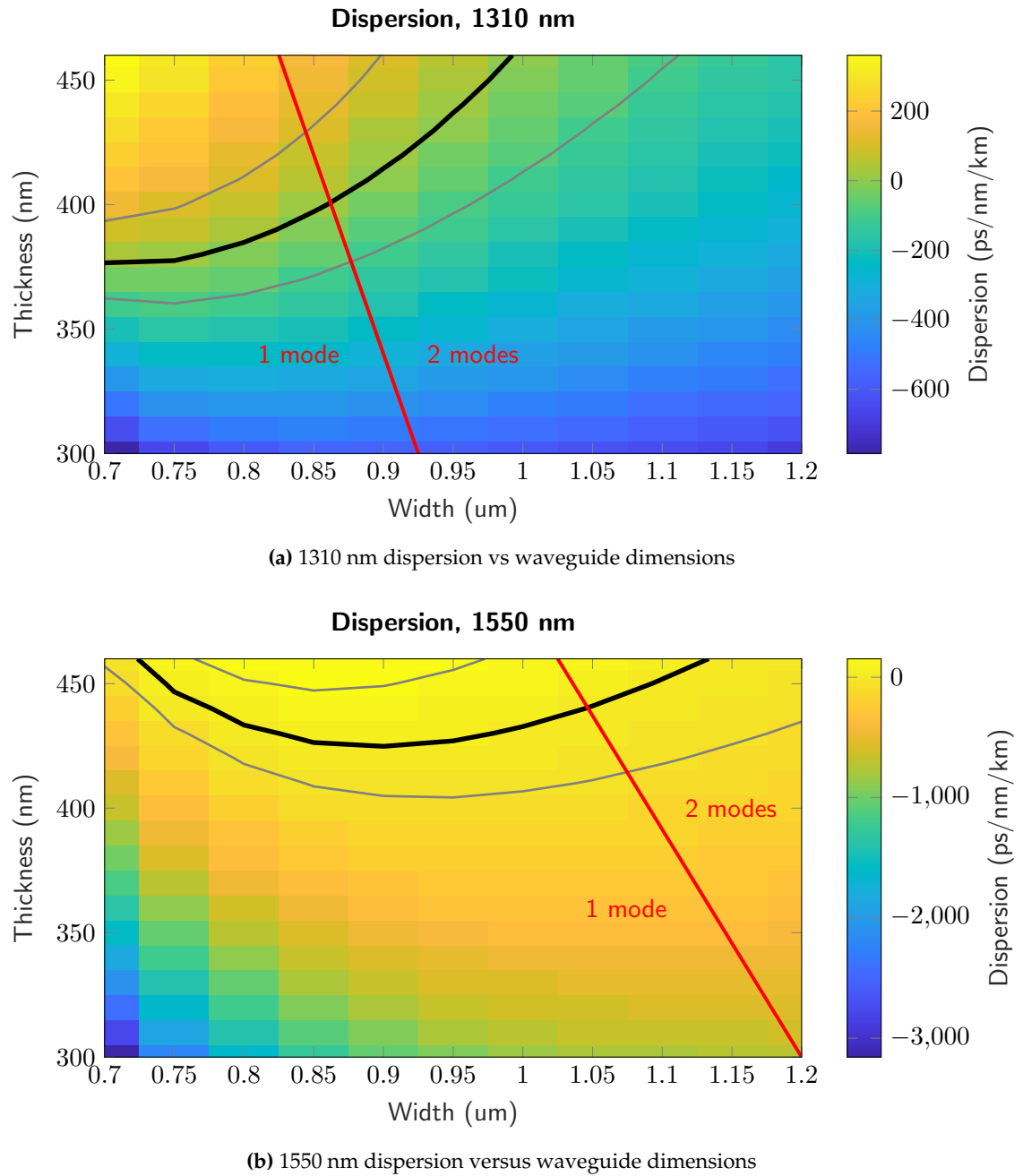


Figure 3.2: Dispersion for differing waveguide widths and heights for 2 wavelengths. The black line indicates points of no dispersion, the grey lines show the points of ± 100 ps/nm/km dispersion. The red line shows the crossover point between a single- and dual-mode waveguide.

to 1550 nm, which shortens the time necessary for the TiO_2 deposition. Later on it was also found that a layer thickness of approximately 400 nm is already pushing the limits of the used etching process, since the etch-selectivity of TiO_2 to the used photoresist mask is just high enough to etch 400 nm of TiO_2 .

The specific dimensions that are targeted for fabrication are the dimensions using the thinnest possible waveguide with no dispersion. This is therefore a waveguide with a thickness of 375 nm, and a width of 0.7 μm . The dispersion will still be below 100 ps/nm/km if the width is up to 0.9 μm , or the thickness of the layer deviates by 15 nm from the desired 375 nm.

Chapter 4

Waveguide fabrication

The fabrication of the waveguides has two main steps. The deposition process to deposit a TiO_2 layer on top of SiO_2 , and the etching process to form individual channel waveguides from the deposited layer. The deposition process was developed almost completely in [23], and adjusted slightly to compensate for tool variation after maintenance. The etching process from [23] is optimized to decrease the sidewall roughness of the waveguides, and to achieve the etch angles of ideally 90° .

4.1 Sputtering titanium dioxide layer

For the deposition of TiO_2 , a sputtering process was used, because it had already been used before in the Optical Sciences group to deposit TiO_2 .

4.1.1 Initial sputtering process used

The initial sputtering process was taken straight from the thesis of I. Hegeman [23]. It is run on the TCOater, in the MESA+ cleanroom at the University of Twente. For reactive sputtering processes, the sample wafer is loaded into a vacuum chamber, in our case facing upwards. Above the wafer, a metal target is mounted. In the chamber, a plasma is created, consisting of argon, and a reactive gas. If it is desired to deposit TiO_2 , a titanium target is used, and the reactive gas in the plasma should be oxygen. The argon ions in the plasma will dislodge metal-atoms from the target upon bombardment, while the reactive oxygen gas will oxidize the metal atom if they interact, forming a TiO_2 molecule. If the molecule happens to hit the sample wafer, the particle can be incorporated into the layer. Due to the pressure necessary to oxidize all atoms however, the particles will diffuse through the chamber. Therefore, they might also wander off target, and hit the sidewall of the chamber, or even hit on the target. These surfaces are therefore also coated during sputtering. On the target, this redeposition can be knocked off again by the plasma.

The most important parameter in a reactive sputtering process is the amount of reactive species in the plasma. If there is too little, not all metal will oxidize before

hitting the sample wafer, causing the deposited layer to be partially metallic. Presence of metal in the layer is detrimental for waveguiding applications, as metal causes high absorption losses. Increasing the oxygen flow will reduce the sputtering rate though, since the target will become more heavily oxidized, increasing the resistive losses in generating the plasma, and therefore reducing the plasma-energy.

To tune the reactive species amount, the sputtering curve is a valuable tool. The curve shows the bias voltage between the metal target and the sample wafer at a fixed plasma power, as a function of amount of reactive species in the plasma. The bias voltage is generated because the current through the plasma experiences resistance between the metal target and the sample. This resistance is affected significantly by the amount of oxidation of the target, where more oxidation causes higher resistance. It follows from the equation $P = \frac{V^2}{R}$ that for a fixed power, the voltage rises with the resistance. The curve that I. Hegeman measured in [23] is reprinted in Fig. 4.1. The final value of the amount of oxygen that was used was on top of the 'shoulder', at an oxygen fraction of 0.135 in the graph. To the left of the shoulder, the layer will be partly metallic, and therefore have low resistance/bias voltage. To the right of the shoulder, the titanium atoms will be completely oxidized, resulting in completely oxidized layers on the sample wafer. The deposition-rate will however reduce the further to the right of the graph you go. Just on top of the shoulder, the process will have the highest deposition rate, but still have completely oxidized layers. The usual bias voltage seen using these settings was a voltage around 410 volts. The difference with the bias voltage shown in the sputter curve in Fig. 4.1 is attributed to target wear. The plasma color visible was always purple.

Using the Woollam M-2000UI ellipsometer, the thickness and refractive index of grown layers has been measured, to determine the deposition rate and layer quality. The deposition rate varied between 1.6 and 1.8 nm/min, the refractive index of the resulting layers at 628 nm varied between 2.37 and 2.47. The source of this variation is not found yet.

4.1.2 Process adjustment after target replacement

During the time of my experiments, the titanium target used in the machine had reached the maximum number of working hours. Therefore, it had to be replaced with a new one. This meant the process had to be readjusted for the new target. Over the lifetime of a target, its shape changes. A picture of a used target is shown in Fig. 4.2. A new target will look completely flat. There are two main differences between the old and new target:

- Trench formation: The plasma digs a trench around the center of the target. This increases the surface area exposed to the plasma.
- Target sagging: The titanium target starts sagging during use. This reduces the contact area with the electrodes. Therefore, the resistance for the plasma current path increases, reducing the sputter rate.

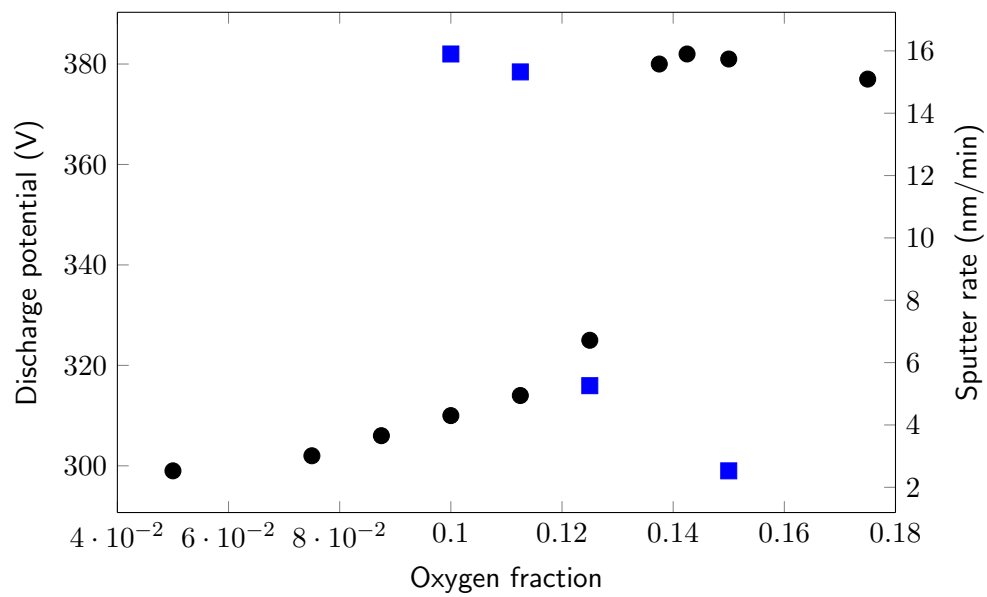


Figure 4.1: Sputtering curve, showing the bias voltage (black circles) and deposition rate (blue squares) as a function of oxygen fraction in the gas flow



Figure 4.2: Photograph of a used sputtering target. A new target is completely flat.

After trying the first run with the new target, using the same settings as with the old target, the plasma color and bias voltage were off. The plasma color was cyan, instead of the expected purple, while the bias voltage was below 400 V. The amount of oxygen was increased, from 6 sccm to 7.5 sccm. This setting resulted in the original purple plasma color, and a bias voltage oscillating between 414 and 417 V. The resulting deposition rates and refractive indices of the layers from the adjusted process were within the variation of the previous process: refractive index at 628 nm between 2.37 and 2.47, and a sputter rate between 1.6 and 1.8 nm/min.

Of course, the process won't be stable after this adjustment, since the new target will deform just as well. This will likely reduce the sputter rate, which can be restored by reducing the oxygen content in the plasma. At some point, the target will have a condition close to the old target, after which the initial process used in [23] using 6 sccm oxygen would work as before. Therefore, the process will have to be calibrated regularly if a stable process is necessary.

4.1.3 Surface roughness of layers

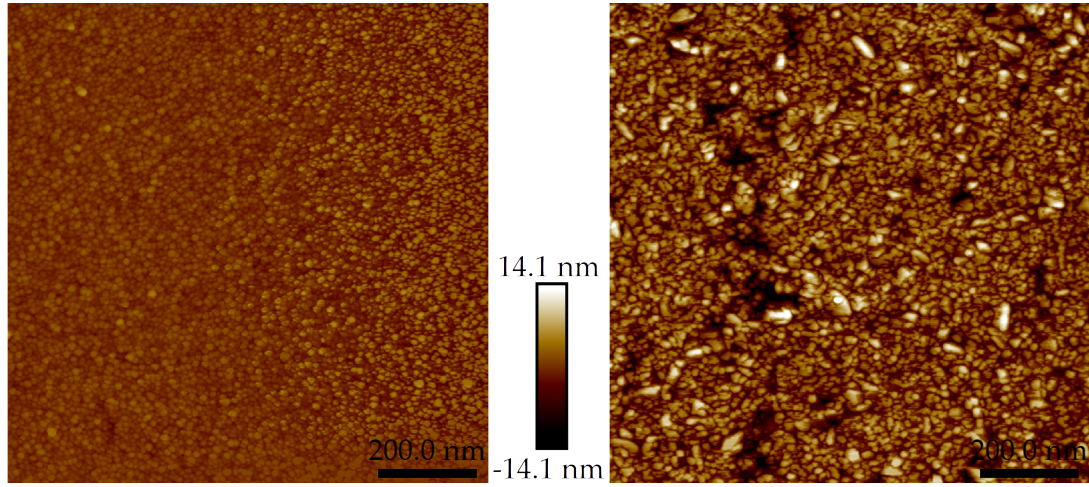
The surface roughness of two TiO₂ layers has been characterized using AFM measurements. Using the M-2000UI ellipsometer, the layer thicknesses were determined to be 83 nm and 360 nm. The propagation losses of waveguides etched in these layers have also been measured, as detailed in section 5.2.2.

The AFM images were taken of a 1 μm \times 1 μm square, with 512 points per line. This means the expected lateral tip-limited resolution of 3 nm is reached in this measurement. The vertical measurement range was set to 200 μm , which gave the highest possible vertical resolution, while saturating the detector only near the edges of the measurement square due to wafer tilt. The resulting surface profile after correcting for wafer tilt and bow can be seen in Fig. 4.3. The quantitative roughness results are shown in Table 4.1.

Table 4.1: Quantitative results of AFM roughness measurements, after correcting for wafer tilt and bow.

Layer thickness (nm)	83	360
RMS Roughness Rq (nm)	1.50	3.93
Maximum height difference (nm)	12.1	35.5
Surface area difference (%)	20.6	52.6

Fig. 4.3 shows that the top surface of both samples are different. The most obvious difference is the roughness amplitude difference between both samples. Another difference is the shape of the peaks and valleys. In the 83 nm thick sample, the peaks and valleys are roughly circular, and the surface seems ordered. The thicker 360 nm sample however, has bigger chunks resembling rice-grains on the surface, which lie on top of a pattern very similar to the thinner sample. The chunks look similar to the features



(a) AFM image of 83 nm thick waveguide surface. The lower 10 percent of the image has saturated pixels on peaks.

(b) AFM image of 360 nm thick waveguide surface.

Figure 4.3: Surface roughness images of two waveguides with differing thickness.

seen in the AFM surface roughness measurement on anatase TiO_2 in [24], These measurements, combined with Raman measurements detailed in Section 5.3.1, lead to the assumption that these bigger chunks are crystal grains of anatase TiO_2 , while the rest of the sample is likely to be amorphous.

4.2 Etching of titanium dioxide

In order to define waveguides in the sputtered TiO_2 layer, most of the TiO_2 needs to be etched away, while leaving the waveguide regions unetched. In order to define waveguides with sharp edges, a dry etching method is preferred, since it can etch directionally. Due to the availability in the MESA+ cleanroom, a recipe was developed for etching the TiO_2 layers in an Oxford PlasmaPro 100 Cobra machine. In order to be able to fabricate waveguides close together, for couplers for example, an etching recipe that leads to sidewalls perpendicular to the surface of the sample is desired. To reduce the propagation losses in waveguides, the recipe should not introduce significant sidewall roughness, which leads to increased scattering losses.

4.2.1 Location selective etching principle

Most etching techniques cannot etch locally, but can only etch a large area at once. In order to end up with waveguides in a deposited layer, this layer can be etched selectively. By protecting the parts of the layer that have to be the waveguide, and not protecting the parts that are undesired, the entire wafer can be etched at once, while only removing the undesired material. Photoresist, patterned using photolithography, is used in

this process. The process steps to apply and pattern the resist are given Appendix A.3.

4.2.2 ICP RIE etching mechanism

The Oxford PlasmaPro 100 Cobra is an Inductively Coupled Plasma Reactive Ion Etching (ICP RIE) machine. The RIE part refers to the etching mechanism. In an RIE process, a plasma containing (a combination of) gasses is generated above the sample in a vacuum chamber. An RF voltage is applied between the sample and the top of the chamber to accelerate the ions generated in the plasma towards the substrate. Upon hitting the sample, these ions will etch the sample in two ways: Physically and chemically. The physical part is caused by the kinetic energy of the ions, which removes material through sputtering. The chemical part enhances this physical component if the ions can react with the sample to form volatile species. These volatile species are then pumped out of the vacuum chamber.

4.2.3 Etch rate measurement method

The etch rate is one of the key aspects of an etching recipe. To determine the etch rate of TiO_2 , a Dektak profilometer was used. Depending on the layer thickness, a different method was used.

Thick layer measurements

In a selective etching process, two etch rates are important: The sample material etch rate, and the photoresist etch rate. These can both be determined using only one sample, and a profilometer. Three profile measurements are taken at the same position on the sample at different points during the process:

1. $H_{\text{pre-etch}}$ Between the lithography step and the etching step
2. H_{etch} Between the etching step and the resist stripping step
3. H_{final} After the resist stripping step.

The amount of sample material etched is simply equal to H_{final} , as it's the measurement of the final product. The amount of photoresist etched is equal to $H_{\text{pre-etch}} - H_{\text{etch}} + H_{\text{final}}$. Finding the etch rate is done by dividing the etch depth by the etch time.

Thin layer measurement

If a layer is etched for a time long enough for the entire top layer to be removed, the layer below that one will start to be etched as well. This process of etching the layer below the targeted layer is called over-etching. When over-etching occurs, the measurement method for thick layers can no longer be applied, since the etch rate is not constant during the etching process. The etching rate is dependent on the material etched. To still be able to measure the etch rates for thin layers that are over-etched, the etch was

run with two samples at once: One sample contained the photoresist mask on a thin layer of TiO_2 , on top of a layer of $8\text{ }\mu\text{m}$ SiO_2 . The other sample was an unpatterned sample with an $8\text{ }\mu\text{m}$ layer of SiO_2 . In addition to measuring the same three heights as in the thick layer method, the SiO_2 layer thickness of the bare sample was measured before and after etching using ellipsometry. Once the etch rate for SiO_2 is known, the three step height measurements are enough to know the etch rates of all three layers in an SiO_2 - TiO_2 - Photoresist stack. The amount of SiO_2 etched in the process can be calculated by subtracting the TiO_2 layer thickness from H_{final} . Since the etch rate for SiO_2 is known, the time it took to etch this part of the sample is also known. The TiO_2 etch rate is then given by dividing its initial thickness by the calculated remaining time. Calculation of the photoresist etch rate remains unchanged.

4.2.4 Etching settings starting point

Following a process proposed by Oxford Instruments, a plasma consisting of Ar, SF_6 and O_2 was used by I. Hegeman in [23] to etch the sputtered TiO_2 layers. The parameters used were as follows:

Table 4.2: Starting point etch settings, from [23]

Parameter	Setting
SF_6 Flow rate	25 sccm
O_2 flowrate	6 sccm
Ar flowrate	5 sccm
Pressure	40 mTorr
ICP power	1850 W
HF power	20 W
Temperature	10 °C
Time	15 min

The resulting waveguide after etching for 15 minutes is reprinted in Fig. 4.4. The initial etch process caused severe sidewall roughness on the waveguide. This is likely due to the poor resist-to- TiO_2 selectivity of the process, and the poor directionality of the etching process. Any irregularities in the resist sidewall profile are quickly amplified if the resist etches fast compared to the TiO_2 . If there is a small hole in the resist sidewall, it quickly becomes a large hole due to the high resist etch-rate, therefore exposing the TiO_2 at the side of the waveguides to the etching. A low etch-directionality amplifies this effect even more, since the resist will be etched away from the sides more quickly..

4.2.5 Tested etching settings variations

To reduce the etch rate and increase the directionality of the etch, several changes were made to the etching settings. The ICP power was reduced from 1850 W to 1500 W to

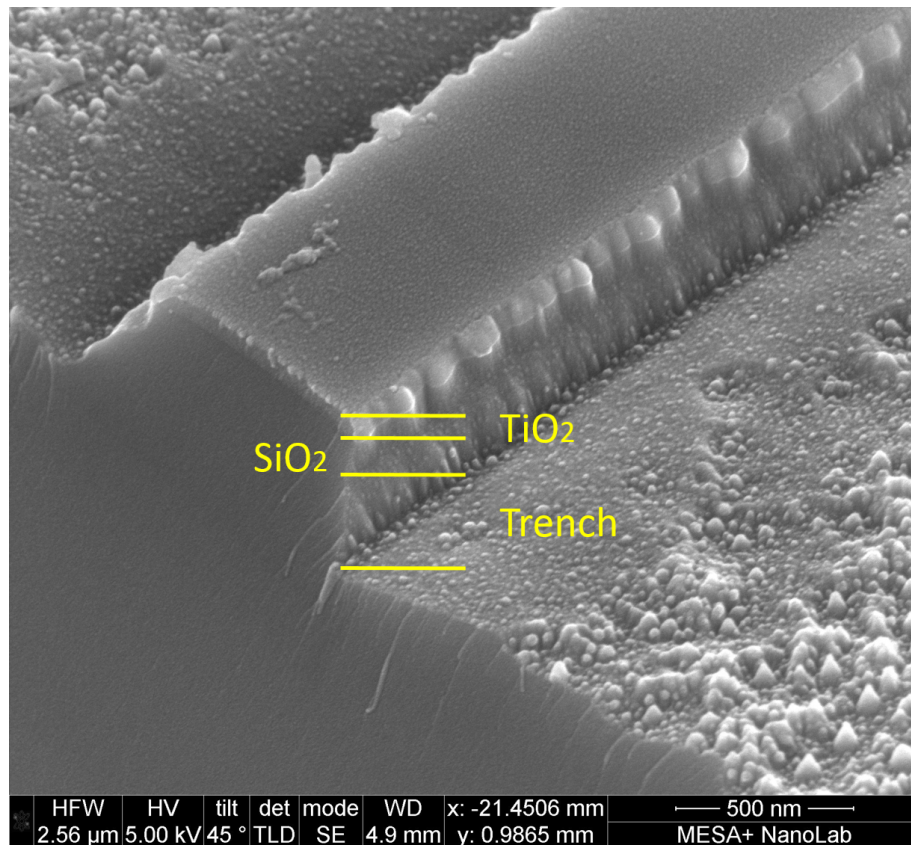


Figure 4.4: Waveguide etched in [23] using initial settings in Table 4.2 for 15 minutes

reduce the plasma power, and therefore the overall aggressiveness of the process. Two extra measures were taken to reduce the etch rate and increase the directionality: Firstly, the pressure was reduced to 10 mTorr. Reducing the pressure increases the mean free path for the ions, reducing the amount of ions that will hit the waveguide from the side, after deflecting off of another ion or other species in the chamber. Secondly, a combination of three different HF powers and three different O₂ flows were tested, which are given in Table 4.3. Increased HF powers could increase the sidewall angle, since the vertical speed of ions will be higher, causing less ions to hit the sample slightly sideways. The reduced amount of O₂ might decrease the etch rate of photoresist, since it is easily etched by O₂.

All tested settings are summarized in Table 4.3.

Table 4.3: Initial etch settings variations

Parameter	Setting
SF ₆ Flow rate	25 sccm
O ₂ flowrate	0 sccm, 2 sccm and 6 sccm
Ar flowrate	5 sccm
Pressure	10 mTorr
ICP power	1500 W
HF power	20 W, 40 W and 60 W
Temperature	10 °C
Time	3 min

These etch recipes were tested on a 65 nm thick TiO₂ layer deposited on 8 μm of SiO₂. This wafer was patterned with waveguide structures ranging from 1 μm to 10 μm in width, following the process flow in Appendix A.3. This patterned wafer was cleaved into 18 pieces of approximately 1 cm by 1 cm. For each etch run, two of those pieces, and another piece of unpatterned 8 μm SiO₂ deposited on Si were glued close to the center of a Si carrier wafer using Fomblin oil. Etch rates for the TiO₂ and resist were determined using Dektak profile measurements before and after etching, and a third profile measurement was done after stripping the resist. SiO₂ etch rates were determined using ellipsometry measurement before and after etching.

Etch rate results on 65 nm TiO₂ layers

The etch rates for the TiO₂, SiO₂ and the photoresist were measured for all combinations of settings in Table 4.3, except for the 6 sccm combined with 40 and 60 W HF power. The measured etch rates are given in Table 4.4

Waveguide etch profiles

In order to check the sidewall profile of an etch, a Scanning Electron Microscope (SEM) with a Focused Ion Beam (FIB) option was used. The FIB allows to dig a trench into the sample, allowing to see a cross section of an etched waveguide with the SEM.

A FIB works by accelerating gallium ions towards a focus on the surface of the sample. Upon impact with the surface, these etch away the material in the focus. This technique does not produce sharp angles on the surface, the edges of a cut will always be rounded. To prevent this rounding from affecting the waveguide, a strong material can be deposited on the sample first. This strong material will then be at the edge of the cut, and become rounded, while the waveguide under it will have a straight cut. In the used FIB, a layer of platinum can be deposited. After the deposition of the platinum, a FIB pattern called 'cleaning cross-section' is used to dig a hole into the sample that allows a clear view of a cross section of the sample.

Since the samples under investigation have a non-conductive surface (both TiO_2 and SiO_2 are insulating materials), they show low resolution in a SEM, due to the surface accumulating a negative charge by electron bombardment (or a positive charge by gallium ions if the FIB is used). If this charge is not conducted away, the charged sample will start repelling electrons, and therefore become invisible for SEM. To counteract this charging effect, the sample can be coated with a conductive layer. A mix of gold and palladium (Au/Pd) is often used for this purpose. Using the Polaron 2011 SEM coater in the Nanolab, a 5 nm layer of Au/Pd was deposited on the sample. The sample is then stuck to the SEM sample holder using conductive carbon tape to allow an electrical path from the sample to ground. Then the FIB can be used to make the cross section.

The waveguide sidewall angles were checked in the SEM for some of the etched waveguides. It was done to check the difference between different O_2 flows at a fixed HF power. The etch profile of each sample etched with 20 W HF power can be seen in Fig. 4.5. The TiO_2 etch profile cannot be characterized in these pictures, since the layer of TiO_2 is so thin there is almost no sidewall. The SiO_2 etching sidewall can be seen, and is not dependent on the O_2 flow.

Etch results on 360 nm layers

In order to characterize the sidewall profile of TiO_2 etching, instead of the SiO_2 etching, two of these settings were tested on a 360 nm thick layer of TiO_2 . For this, the combination of 6 sccm O_2 flow and 20 W HF power and the combination of 2 sccm O_2 flow and 20 W HF power were chosen. The first was chosen since it was the setting closest to the recipe proposed by Oxford Instruments, and the second was chosen for its highest selectivity of TiO_2 to photoresist. Etch profiles resulting from both of these settings are shown in Fig. 4.6.

The etching profile of the etch variation with an O_2 flow of 6 sccm in Fig. 4.6a is very close to the desired etching profile with a 90° sidewall angle. The sidewall angle in the shown picture is around 76° for the left wall, and 86° for the right wall. The etch

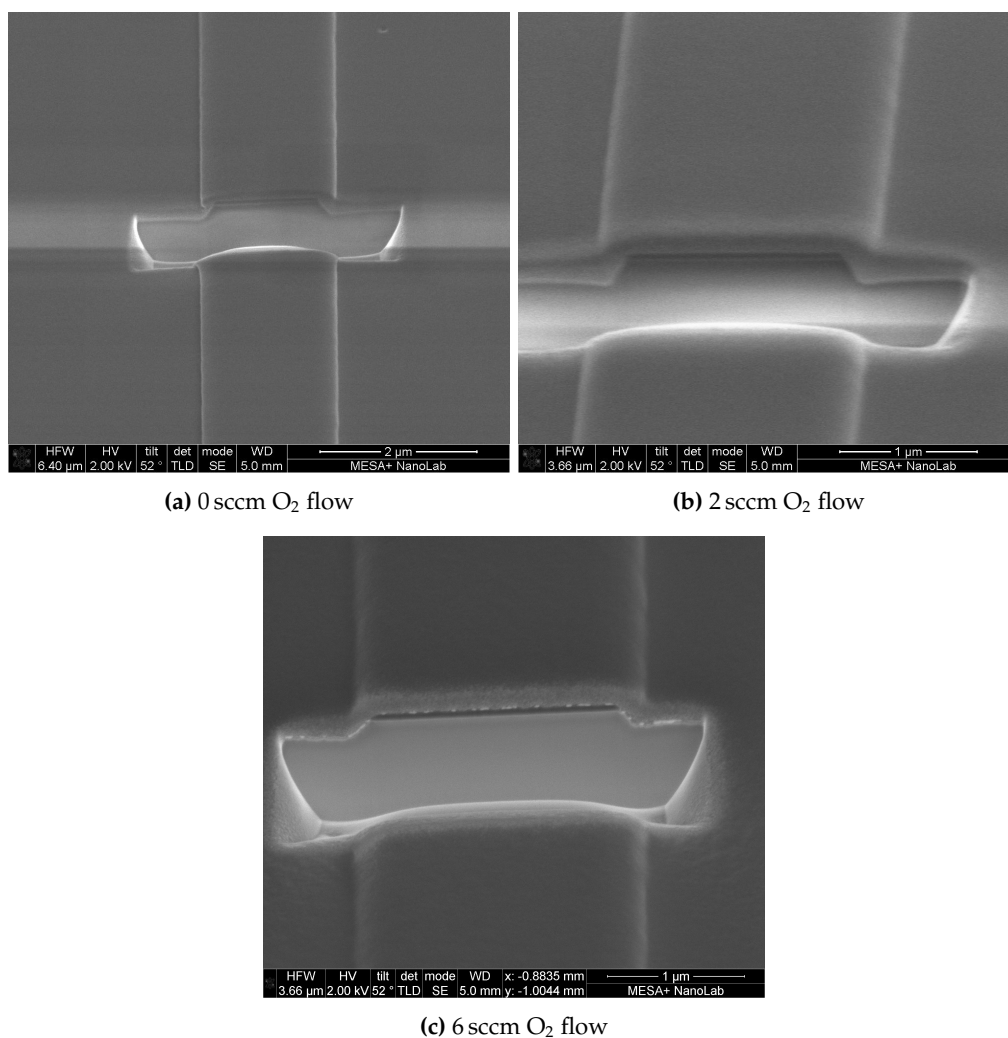
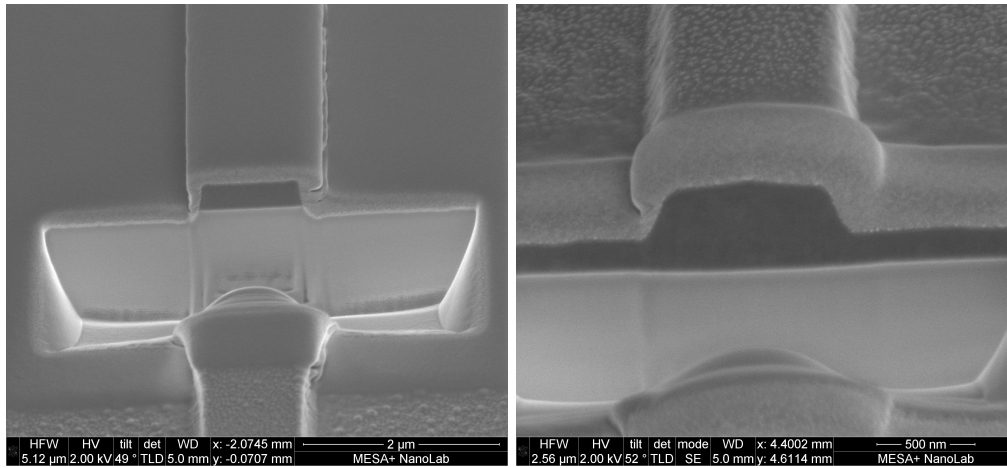


Figure 4.5: Etch profile of 65 nm TiO₂ layers on 8 μm SiO₂ samples etched at 20 W using the settings in Table 4.3, with varying O₂ flows. In each image, the thin dark line on the cross section is the TiO₂ on top of SiO₂. A platinum layer was deposited on top of the TiO₂ to prevent FIB rounding effects.

Table 4.4: Etch rates and selectivities of initial etch settings test on 65 nm TiO₂ layers.

(a) TiO ₂ etch rates in nm/min				(b) SiO ₂ etch rates in nm/min			
HF power (W)	O ₂ flow (sccm)			HF power (W)	O ₂ flow (sccm)		
	0	2	6		0	2	6
20	68	72	55	20	77	71	61
40	83	69	n/a	40	96	89	n/a
60	93	117	n/a	60	109	99	n/a
n/a: Settings not tested				n/a: Settings not tested			
(c) Resist etch rates in nm/min				(d) TiO ₂ to resist selectivity			
HF power (W)	O ₂ flow (sccm)			HF power (W)	O ₂ flow (sccm)		
	0	2	6		0	2	6
20	244	267	245	20	0.28	0.31	0.23
40	334	322	n/a	40	0.25	0.21	n/a
60	411	401	n/a	60	0.23	0.29	n/a
n/a: Settings not tested				n/a: Settings not tested			

**(a)** 6 sccm O₂ flow, etched for 5:20 minutes.**(b)** 2 sccm O₂ flow, etched for 5:30 minutes**Figure 4.6:** Etch profile of 360 nm TiO₂ layers on 8 μm SiO₂ samples etched at 20 W using the settings in Table 4.3, with different O₂ flows and etching times. A platinum layer was deposited on top of the TiO₂ to prevent FIB rounding effects.

depth is equal along all exposed SiO_2 in the cross section, except for a small amount of trenching around the waveguide. The top of the waveguide is also flat.

The etching profile of the etch variation with an O_2 flow of 2 sccm in Fig. 4.6b is considerably worse compared to the other trial. The etch did not go completely through the TiO_2 layer, but the etch time chosen was the maximum time that could be etched before the photoresist mask would be etched away completely. The images seem to suggest the used etching time was too long, as the top of the waveguide is not flat anymore, but has a triangular shape. If the surface below the photoresist mask is affected by the etch, the photoresist has been etched away completely during the etching process. The triangular shaped top of the waveguide is likely caused by the photoresist having a triangular shape after development and hardbaking. In this case, the resist close to the sides is thinner, and therefore, etched away more quickly. The center of the waveguide is protected the longest, and therefore etched the least.

The result shown in Fig. 4.6b raise questions regarding the etch rate measurements done on thin layers in section 4.2.5. From the etch rates measured on thin layers it was expected that entire TiO_2 layer would be etched through, but it has not. This could mean that the original measurement is incorrect, or the etch behaves differently depending on the etching time. A reason for this different behaviour could be heating of the sample during etching. The faster (2 sccm O_2) etch likely heats up the sample faster, since the etching process is quicker. This could explain why the slower etched worked as expected for a longer time, and the faster etch did not.

4.2.6 Chosen etch recipe characteristics

Following the results of the etching variations, the settings using 6 sccm O_2 and 20 W HF power were selected as the optimal settings. These settings lead to a waveguide sidewall angle that is close to 90° , with a selectivity of TiO_2 to photoresist that allowed etching waveguides with the desired thickness of up to 400 nm. To gain more confidence in the performance of the etching process, the etch rates were determined for several etching times. Also, the etching profile was checked for several waveguide widths.

Etch rates

The etch rates were tested on a sample with a 400 nm TiO_2 layer. Initially, 4 etch runs were done, with etch-times of 40 s, 80 s, 120 s and 160 s. From these 4 points, the etch rate was extrapolated to find the time necessary to etch the entire layer, with 5% extra etch time to ensure a complete layer etch with a small amount of overetching, resulting in an etch time of 5:20 minutes.

Using the Dektak method explained in Sec. 4.2.3, the etch rates for TiO_2 and photoresist were measured for each of these measurements. The measured etch depths as a function of etch-time and their linear fit can be seen in Fig. 4.7. The etch rate for TiO_2 and the used photoresist are 81 ± 4 nm/min and 219 ± 4 nm/min respectively. These

rates were all measured on different pieces cleaved from the same wafer. The variation of the etch rates between different layers has not been tested.

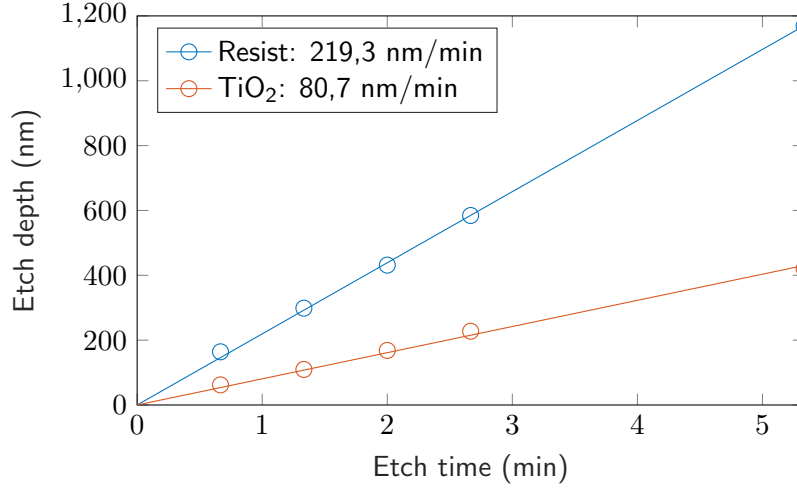


Figure 4.7: Resist and TiO₂ etch rates of the recipe in Table 4.3, using 20 W HF power, and 6 sccm O₂.

Etch profiles

The etch profiles were examined for mask widths of 0.8 μm , 1.2 μm and 1.6 μm . The results are shown in Fig. 4.8. It can be seen the sidewall angle is not dependent on the width of the waveguide. The measured sidewall angles in these SEM images are between 76.6° and 86.6°, with an average of 83.7°.

Fig. 4.8 also shows that the etched waveguides are narrower than the mask width, showing an etch bias. In this case, they are 0.2 μm thinner. The narrowing on a sample with a thin TiO₂ layer that was etched for 1 minute and 10 seconds was only 15 nm as measured from a SEM image. Therefore, it can be assumed the waveguides are etched from the side during the etching process, and it is not caused by the lithography process. In these waveguides, the 100 nm etching on both sidewalls happened in 5 minutes and 30 seconds, resulting in a sidewall etchrate of $100/5.5 = 18.2 \text{ nm/min}$, showing that the thinning is not caused by the lithography process.

Etch uniformity over wafer

The uniformity of the etch was tested on a bare layer of TiO₂. The thickness of the TiO₂ ranged from 88 to 74 nm prior to etching. It was then etched for 35 seconds. The extracted etch rates as a function of wafer position are plotted in Fig. 4.9.

What stands out in this measurement is the fact that the measured etch rate in the center of the wafer is only 62 nm/min, 75% of the value measured in Fig. 4.7. This difference could be caused by the fact that for the uniformity measurement, a full wafer

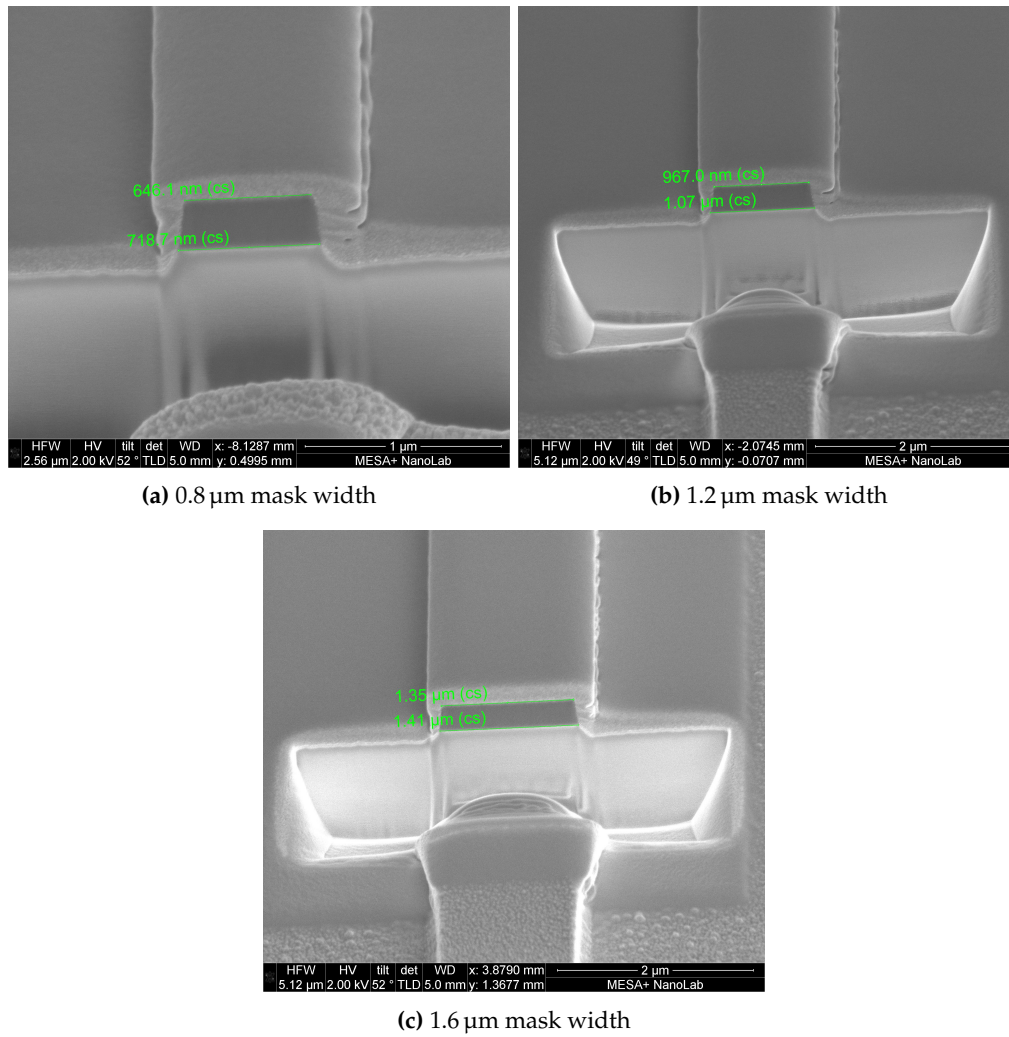


Figure 4.8: Etch profile of 360 nm TiO_2 layers on 8 μm SiO_2 samples etched using the optimal etch settings for 5 minutes and 30 seconds. The mask width is varied in each picture

was etched, instead of a sample stuck to a p-doped silicon carrier wafer. Therefore, the distance from the plasma is one wafer thickness (0.55 mm) longer, but also the thermal and electrical properties change. This might have caused a reduced etch rate. Also, it could mean that the TiO_2 layer used had different properties.

The uniformity of the etch met the requirements for the mask design used. For positions within 3 cm from the wafer center, the etch rate is within 0.5% of 62 nm/min. In the mask used to etch waveguide chips, all waveguides are within this region. Therefore, the entire TiO_2 layer can be etched through for each chip.

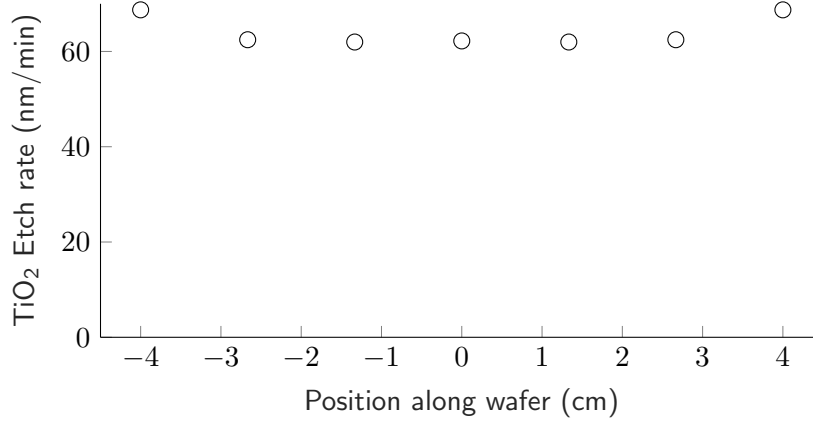


Figure 4.9: Etch rate along the diameter of the wafer.

4.3 Summary and conclusions

In this chapter, fabrication recipes have been introduced that can make waveguides in TiO_2 on SiO_2 . The entire process flow is given in Appendix A. The reactive sputtering process recipe was taken from [23], and slightly modified to account for tool variation. It deposits TiO_2 layers with a refractive index at 628 nm between 2.37 and 2.47, deposited with a deposition rate of 1.6 nm/min to 1.8 nm/min. The layers likely contain a mix of polycrystalline anatase and amorphous TiO_2 .

The etching process was taken from [23] as well, and several variations were tested to achieve the highest sidewall angle. The final recipe leads to sidewall angles between 78° and 86° . The TiO_2 etch rate was measured to be around 81 ± 4 nm/min for samples stuck to a carrier wafer, and was measured in a single measurement as 61 nm/min when full wafers were etched. The selectivity of TiO_2 - to photoresist etch-rate was measured to be around 0.3.

Both recipes together should allow the waveguide design proposed in Section 3.1.1 to be fabricated.

Chapter 5

Waveguide Characterization

To assess the performance of the fabricated waveguides, several characterizations were done. The most important aspect of the waveguides is the propagation loss, which is measured at several wavelengths. Also, the Raman spectrum of the waveguides is measured, to analyse the morphology of the TiO_2 .

5.1 Measurement methods

The two measurements that were repeated for several waveguides were measurements of the propagation losses, and of the Raman spectrum. Those measurement methods are explained in the following sections.

5.1.1 Propagation loss measurement

The measurement of waveguide losses was done using a camera. For wavelengths below 1000 nm, a CMOS camera from Clearvision was used, for wavelengths above 1000 nm the Xenicx Bobcat-320 InGaAs camera was used. Light was coupled into the waveguides from one of the end-facets of the waveguide, and a picture was taken from the top of the sample. From the picture, an exponential decay can be fitted to the intensities along the waveguide, giving the propagation losses. The MATLAB-script to achieve this is given and described in Appendix B

Several coupling methods were tried. Initially, light was coupled into the waveguides using a single mode fiber with a 9 μm core diameter. Light coupling was possible, but not with a high efficiency, due to the large mode size-mismatch. To improve the coupling efficiency to the waveguide, the fiber was switched for one with a core diameter of 4 μm . The mode area of the mode in this fiber is closer to the mode area in the waveguide. On the other hand, this fiber has a larger cone of light emission. Therefore, a lot of stray light showed up in the image, making exponential fitting more difficult. The third coupling method that was used was coupling a free-space beam using an objective. This gave the best results, with little stray light visible in the image.

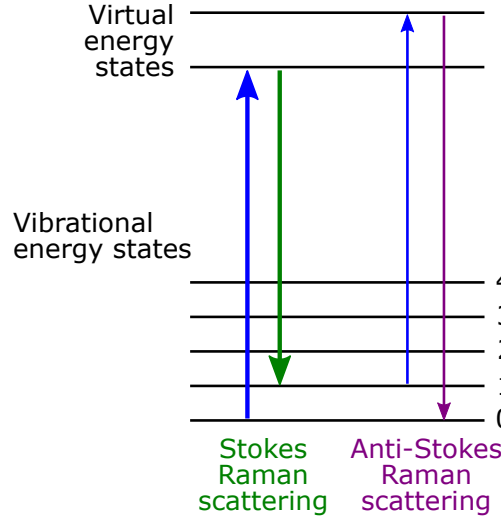


Figure 5.1: Energy level diagram of Raman scattering. Modified from [25].

5.1.2 Raman spectrum measurement setup (Add figure)

Raman spectroscopy gives information about the vibrational and rotational states of a sample, by shining a single wavelength of light into the sample. It is schematically depicted in Fig. 5.1 During interaction with the photons, the system can be excited from a certain vibrational/rotational state to a virtual state with a higher energy by absorbing the photon. Once the system relaxes it can return to either the same or a different vibrational/rotational state than the initial state. In the case of a different state, the wavelength of the emitted photon will be different from the original wavelength. The photon energy shifts that can be observed are therefore dependent on the different vibrational/rotational states of the system. Because crystals have well defined vibrational states, they are easily recognized by their Raman spectrum.

In the used waveguide Raman setup in the Optical Sciences lab, a 785 nm laser is coupled into the waveguide using an objective. The light that is backscattered from the waveguide is collected by the same objective. The light that is collected by the objective is notch-filtered to filter out the light at 785 nm. After this, it passes through a monochromator, where the spectrum is observed by a camera. The spectrum was then mapped to wavenumbers by using the known peak positions of crystalline silicon at 521 cm^{-1} and 950 cm^{-1} [26]. These peaks are present in the measured signal, since part of the light interacts with the crystalline silicon substrate.

Raman spectra of TiO_2 crystals

Each crystal phase of TiO_2 has a different Raman spectrum. The two phases of TiO_2 that have been grown using reactive sputtering in literature are the anatase and rutile phases [22], [24], [27]–[29]. No literature was found where the brookite phase was grown with such a process. The Raman spectra for the rutile and anatase phase have

Table 5.1: Raman spectrum peaks for rutile and anatase TiO_2 , as measured by U. Balachandran and N. G. Error in [30]

Rutile peaks (cm^{-1})	Anatase peaks (cm^{-1})
320-360	398
448	515
612	640
827	796

been measured in [30]. The peaks measured for both crystals are given in Table 5.1. Amorphous materials show no discernible peaks in a Raman spectrum but show a very broad response, while polycrystalline materials will give broadened peaks.

5.2 Initial waveguides characterization

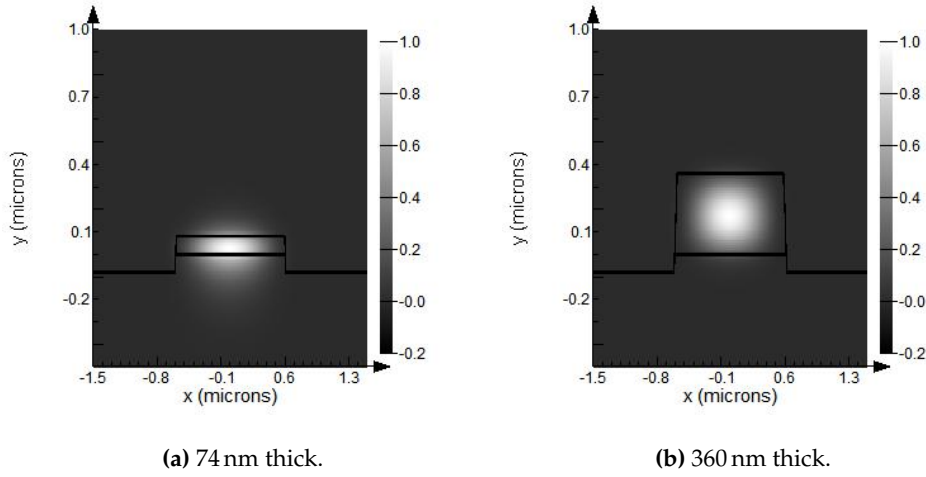
The initial propagation loss measurements were done on two samples with different waveguide thicknesses: One sample had 74 nm thick waveguides, while the other had a waveguide thickness of 360 nm. The 74 nm waveguide thickness was chosen because the 74 nm sample would be single mode at a wavelength of 785 nm, with applications for surface enhanced Raman spectroscopy in mind. The second sample thickness of 360 nm was used because it was the smallest thickness where waveguides with zero dispersion in the O or C band could be achieved with the available lithography. A waveguide ideally has no dispersion at the wavelength of interest in order for four wave mixing to be as efficient as possible, since it will provide full phase matching.

5.2.1 Propagation modes comparison of measured waveguides

The two tested waveguides have different allowed modes. Therefore, a direct comparison between the two waveguides cannot be made. They can however still be compared at a wavelength of 785 nm, since both waveguides support a mode for this wavelength. To still be able to compare measurements between the two waveguides in a fair manner, the amount of their fundamental TE mode power in certain regions was calculated from a mode simulation. The regions of interest for this are the power confinement in the TiO_2 core and in the SiO_2 cladding, since these regions can cause material losses, and 10 nm around the etched sidewall to account for surface scattering. The simulated modes can be seen in Fig. 5.2. The power confinements in the regions of interest are shown in Table 5.2.

Table 5.2: Percentage of power in different areas for fundamental TE mode of two waveguides

Waveguide thickness (nm)	TiO ₂ power (%)	SiO ₂ power (%)	Sidewall ± 10 nm power (%)
360	95	3.5	0.11
75	42	42	0.11

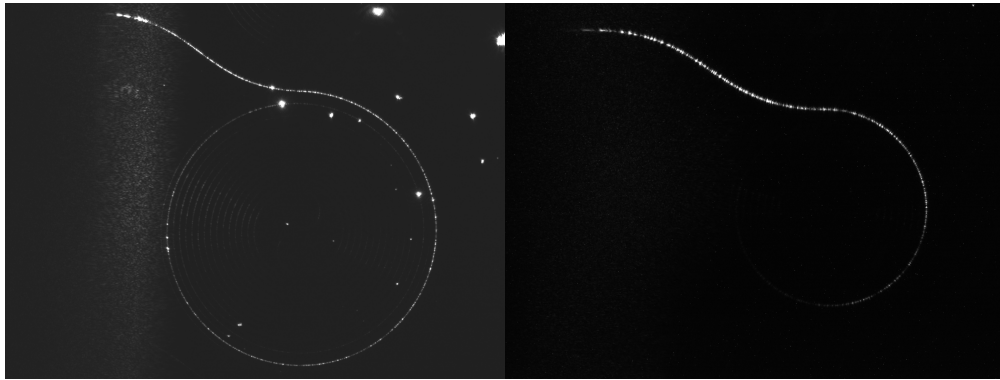
**Figure 5.2:** First order mode calculated for two 1.2 μm wide waveguides of differing thickness.

From the power confinements for different areas, these waveguides were expected to have equal propagation loss contribution caused by sidewall interaction, but differing losses due to the inherent TiO₂ and SiO₂ losses. Expected losses for propagation in TiO₂ and SiO₂ were on the order of several dB/cm, following measurements done by I. Hegeman for propagation losses in slab waveguides of the same materials in [23]. Therefore, both waveguides are expected to have very similar losses, within 1 dB/cm from each other.

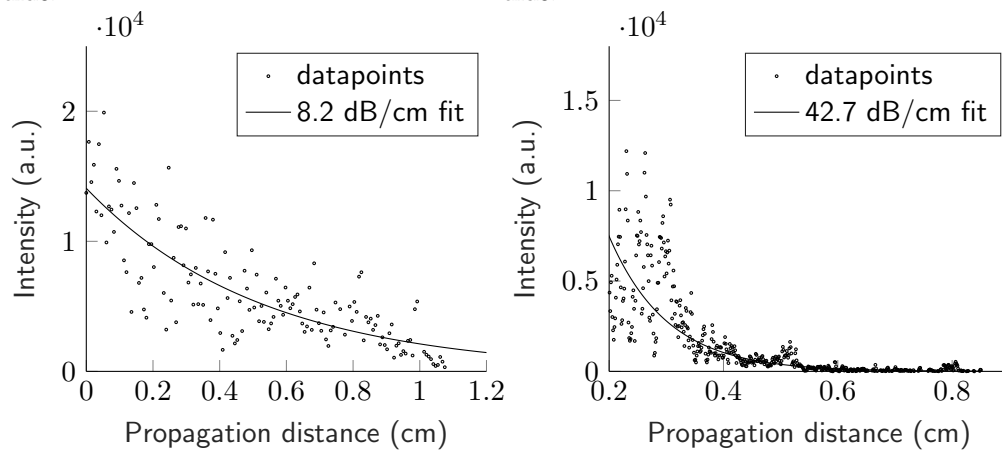
5.2.2 Propagation losses at 785 nm

Using a Ti-Sapphire laser tuned to 785 nm and an objective to couple the light into the waveguides, propagation losses of both the 74 nm and 360 nm thick waveguides were measured. The raw images captured, and the exponential decay fitted to the intensity profile can be seen in Fig. 5.3.

The measurements show a propagation loss of 8.2 dB/cm for the 74 nm thick waveguide, and a loss of 42.7 ± 1.8 dB/cm for the 360 nm thick waveguide.



(a) Raw image of light in 74 nm thick waveguide. (b) Raw image of light in 360 nm thick waveguide.



(c) Exponential decay fit of light in 74 nm thick waveguide. (d) Exponential decay fit of light in 360 nm thick waveguide.

Figure 5.3: loss measurements of a 75 and 360 nm thick spiral waveguide.

5.2.3 Raman spectra of two waveguides of different thickness

The big difference in propagation losses between both waveguides can be caused by a difference in the crystal phase of the TiO_2 in the waveguide. Therefore, the Raman spectra of both waveguides was measured. The results of the measurements can be seen in Fig. 5.4.

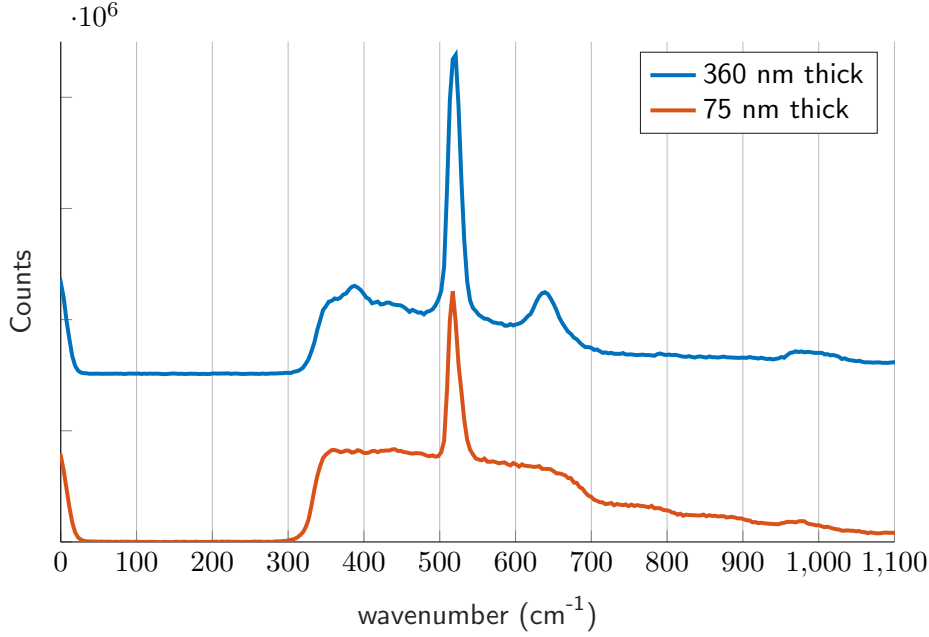


Figure 5.4: Raman signal of two waveguides of different thickness. The peaks at 384 cm^{-1} and 643 cm^{-1} in the spectrum for the 360 nm thick waveguide indicate the presence of anatase TiO_2 .

The spectra of both waveguides show a sharp peak at 521 cm^{-1} . This peak is due to the silicon, which is present in the SiO_2 . Both spectra also show the small and broad silicon peak around 1000 cm^{-1} . The peaks at 384 and 643 cm^{-1} in the Raman spectrum for the 360 nm thick waveguide show that this waveguide contains TiO_2 of the anatase phase, while the lack of those peaks suggests the 75 nm thick waveguide has only amorphous TiO_2 . Since amorphous TiO_2 shows no peaks, it is not possible to know if the 360 nm thick waveguide contains a mix of anatase and amorphous TiO_2 , or only TiO_2 in the anatase phase.

5.2.4 Propagation loss from 1500 to 1635 nm

1550 nm is the most important wavelength for optical communication. For a wavelength of 1550 nm, only the 360 nm thick waveguide supports a mode. Therefore, no comparison can be made between the two waveguides at this wavelength. The main purpose of this measurement is to check whether the losses are mostly surface scattering losses, or

if there's an extra contributing mechanism. These surface scattering losses are theoretically inversely proportional to the wavelength to the fourth power ($\alpha \propto \frac{1}{\lambda^4}$), as shown in section 2.1.1. Measuring the losses as a function of wavelength is therefore a way to extract the amount of scattering losses. The measured losses can be seen in Fig. 5.5.

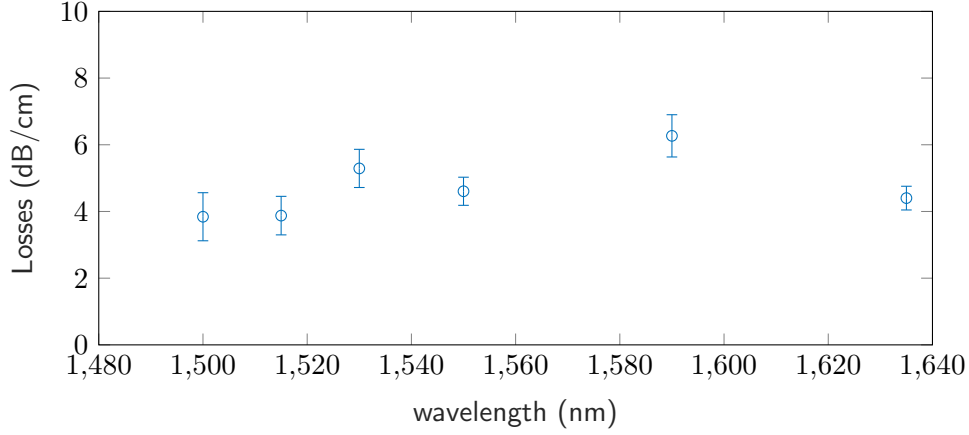


Figure 5.5: Propagation losses around the C-band for 360 nm thick waveguide.

To measure the losses, light was coupled into the waveguide spirals using a small core fiber, with a core diameter of 4 μm . This provided coupling, but there was also a lot of stray light. This made fitting the measured data quite difficult. Therefore, the error (95% confidence interval of the fit) on this measurement is several dB/cm. Due to the stray light however, it was difficult to perform background subtraction in the image. This might mean the actual error is even higher than this, due to fitting a pure exponential to data that contains an exponential plus a constant. It is hard to judge from the resulting plots, due to the high amount of noise in the data.

5.2.5 Analysis of waveguide losses

In the small wavelength window measured below, no $\frac{1}{\lambda^4}$ of the absorption is seen. The comparison can be made with the data point already taken at 785 nm. If the propagation losses are only caused by surface scattering losses, $\alpha_{\lambda=785 \text{ nm}} \times 785 \text{ nm}^4 = \alpha_{\lambda=1550 \text{ nm}} \times 1550 \text{ nm}^4$ should be true, if the model proposed in [18] is correct for our waveguides, and the mode overlap with the side-wall regions is taken into account. If both sides of the equation are filled in, we get a value of $1.62 \times 10^{13} \text{ dB/cm/nm}^2$ at 785 nm, and a value between $2.0 \times 10^{13} \text{ dB/cm/nm}^2$ and $3.8 \times 10^{13} \text{ dB/cm/nm}^2$ in the measurement from 1500 nm to 1635 nm, for the highest and lowest valued data point respectively. Once these values are divided by the mode overlaps with the sidewall, to account for reduced interaction with the scatter points, the values become $3.24 \times 10^{14} \text{ dB/cm/nm}^4$ for 785 nm light, and between $1.25 \times 10^{14} \text{ dB/cm/nm}^4$ to $2.38 \times 10^{14} \text{ dB/cm/nm}^4$

The difference between these two values suggests there is another loss mechanism involved, that is more pronounced at lower wavelengths, or that the sidewall is not the

only region that causes surface scattering. The top surface of the waveguide could also cause scattering losses due to roughness.

5.2.6 OH group absorption

In silica optical fibers, there's an absorption band at 1400 nm, caused by absorption due to a vibrational state transition in hydroxyl (OH) groups [31, Chapter 9]. Also, these groups were found to be present in sputtered Al_2O_3 layers [32]. Therefore, it was checked whether OH groups were present in the grown TiO_2 layers.

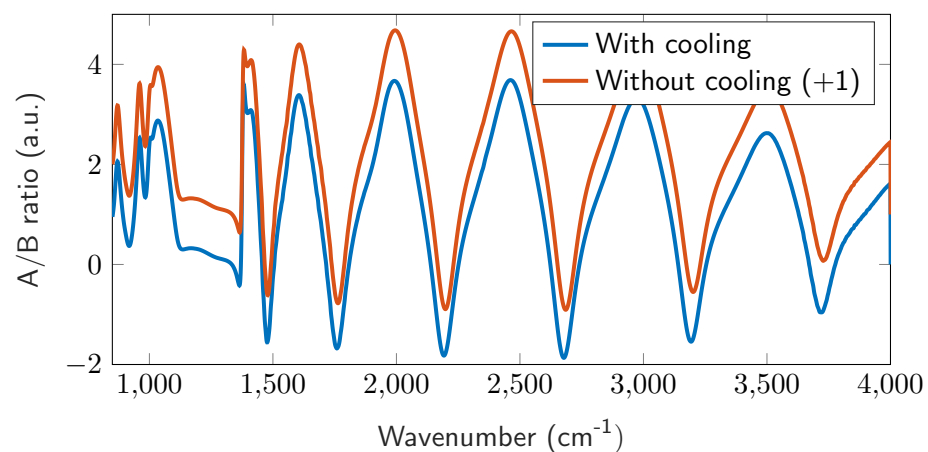
It was expected that OH groups could be incorporated into the TiO_2 layer during deposition via the tool's cooling system. The cooling system on the tool works by blowing atmospheric air onto the bottom of the sample, instead of using an inert cooling gas, or a completely different solution like water cooling. Some of this air could escape from below the wafer into the chamber. The moisture in the air can then be a source for OH-groups that are incorporated into the layer.

Since the OH group absorption is due to a vibrational state change of molecules, they can be detected from their infrared absorption. The OH stretch vibration of SiOH molecules has a strong absorption peak at 3748 cm^{-1} . To easily measure a large part of the infrared spectrum, and to detect possible other vibrational/rotational absorption peaks, it was opted to use the Fourier Transform InfraRed (FTIR) spectrometer of the Molecular NanoFabrication group at the university of Twente. The setup could measure the reflection of both S- and P-polarized light off of a layer, at a given angle. These spectra are called the A- and B-spectrum. Taking the ratio between both polarizations makes sure the absorptions in the air are not measured, since these absorptions are polarization-independent. The absorptions in the layer however, are polarization dependent. The part of the spectrum that was measured ranged from 850 cm^{-1} to 4000 cm^{-1} .

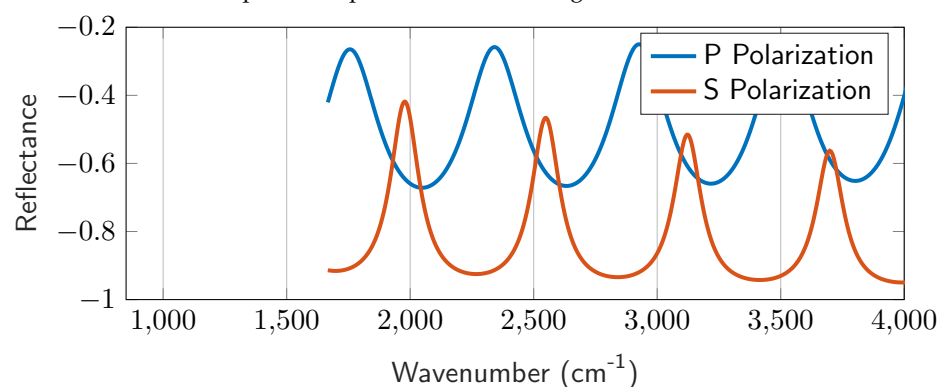
The FTIR measurement for both layers is shown in Fig. 5.6a. It can be seen that both measurements are extremely similar, showing there is no difference between the layer grown with cooling, and the one grown without cooling.

The measurements do have a very different shape from what was expected. The measurement not only shows the absorption spectrum, but also the Fabry-Perot resonances. To check that these features actually were due to Fabry-Perot resonances, the entire film stack's reflectance was calculated in Filmetrics' online reflectance calculator. The reflectance for both polarizations is plotted in Fig. 5.6b. The distance between these fringes is very similar to the fringes in the FTIR measurement.

In one of the measurements done for a smaller part of the spectrum, it was possible to extract an absorption peak from the spectrum. This was done using only the B-spectrum, instead of using the usual A/B ratio. The raw data of this measurement is plotted in Fig. 5.7. It can be seen that the valley at 1480 cm^{-1} does not fit the pattern of peaks and valleys. To better visualize the Fabry-Perot fringes expected in this measurement, a smoothed spline fit was made of the data, while excluding the entire peak around 1480, which is also shown in Fig. 5.7. From this, it is clear there are two absorp-



(a) A/B ratio measured for two grown layers, with and without cooling. The measurement without cooling is offset, otherwise it is not visible behind the other measurement. The A/B ratio is between the signal measured for the S- and P-polarized part of the infrared light.



(b) Calculated S- and P-polarization reflectance for an 88 nm TiO_2 layer under the same angle as the FTIR measurement.

Figure 5.6: FTIR measurement and reflectance simulation for the measured TiO_2 layer.

tion peaks visible in this measurement: At 1483 cm^{-1} and at 2349 cm^{-1} . The first one might indicate the TiH-stretch vibration of HTiO groups [33], while the second one is due to absorption from carbon dioxide in the air [34]. The CO_2 absorption is normally removed by taking the A/B ratio.

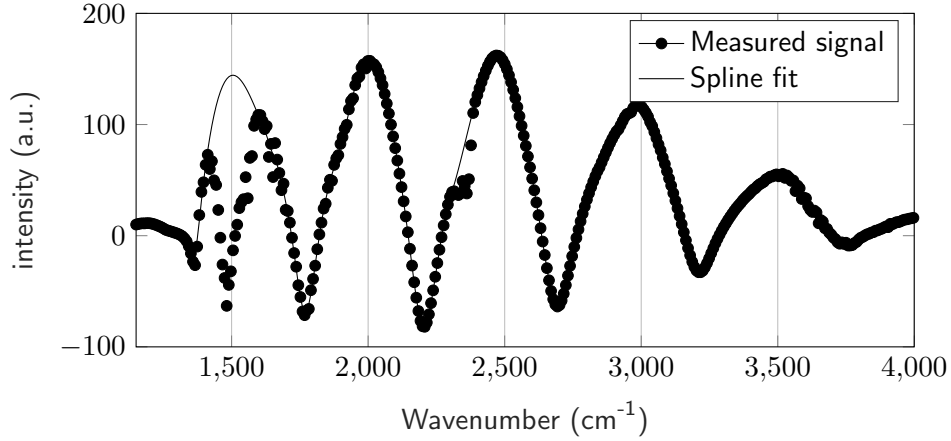


Figure 5.7: Raw B-trace data, and the spline fit.

In none of the measurements, peaks around 3748 cm^{-1} belonging to OH groups were found.

5.2.7 XPS measurements

Using an XPS measurement, the atomic content of samples can be measured. The minimum concentration of an atom necessary for detection is dependent on the atom. Lighter atoms have a higher limit of detection compared to heavier atoms, while hydrogen atoms can not be detected.

Next to giving information on the atomic content of a sample, XPS can also distinguish between the specific bindings of these atoms. For example, Ti, TiO and TiO_2 each show up as slightly different peaks in the measurement. This gave an opportunity to check whether the sputtering process gives results in a pure layer of TiO_2 , or whether the layer also contains Ti or TiO.

The XPS measurement was done on two samples: The 360 nm thick waveguide also characterized in Section 5.2, and a TiO_2 layer right after deposition. These were both inspected, since contamination might be introduced in the deposition- or etching-process. For the inspection, a survey spectrum was measured to see which elements were present in the sample. For all elements present, a more precise spectrum was taken at their prominent peak energies. The measurement report made by the XPS operator is attached in Appendix C.

The XPS results showed that all titanium atoms in the sample are in the form of TiO_2 . In the measurement on the etched waveguide silver showed up as contaminant.

This was present in the topmost 20 nm of the layer. In the blanket layer, no contamination was present. The cleanroom-staff investigated the silver contamination, but no source was found. Due to the costs, no extra XPS measurements were done on different samples, so it's not known whether this contamination is in all waveguides, or only in this one. Other contaminants were not found in the samples.

5.2.8 Discussion

The results of the initial loss measurement were not as expected. The expected difference between the two waveguides based on the power confinements in the sidewall region was within 1 dB/cm, but the actual difference is more than 35 dB/cm. Since the mode overlap with the sidewall is very similar between both samples, this is likely not caused by sidewall roughness. Since the thick waveguide has more mode overlap with the TiO_2 core, it is expected that material losses in the core account for the big difference between the two waveguides. Even though both waveguides had their TiO_2 layer grown with the same process, the temperature during the layer deposition was different between the two samples. Since the 360 nm layer had to grow for longer, the temperature had also increased to a higher level near the end of the deposition than for the 74 nm layer. The TCOater gives approximate wafer temperatures based on the vacuum chuck temperature. Both layer depositions started at an approximate wafer temperature of 25 °C. The 74 nm layer was at a wafer temperature of 34 °C when the deposition finished, while the 360 nm thick waveguide had reached a wafer temperature of approximately 54 °C by the end of the deposition. Furthermore, the etching step took longer for the thicker waveguide as well. It is not known what temperatures are reached during etching, nor if they are higher for the 360 nm thick sample compared to the 74 nm thick sample.

Crystallization of the TiO_2 can occur at higher temperatures. No distinct crystallization temperature threshold was found in literature. Many values are listed for the transformation from the amorphous to the anatase phase in an annealing step, ranging from 180 °C to 450 °C [35]–[37]. Information about crystallization as a function of process temperature for a sputtering process could not be found. From measurements done by I. Hegeman in [23], it is found that increasing the temperature during the deposition causes the layer losses to increase. Deposition at 25 °C causes layer losses below 1 dB/cm, while growth at 100 °C causes losses of 8 dB/cm, which could be caused by the effects of crystallization.

The FTIR shows the waveguides do not contain OH groups, which means the losses at 1550 nm can not be reduced by limiting the OH groups in the material. The XPS measurements have shown that all Ti in the layer is completely oxidized into TiO_2 , showing the losses in the waveguides are not due to metal absorption of Ti. This does not match what was expected from FTIR measurements, since they seemed to show HTiO groups. This might be caused by the fact that HTiO and TiO_2 have very similar XPS responses. No reference XPS spectra were found for HTiO.

5.3 Effects of deposition and etching time on morphology and propagation losses

The samples measured earlier in Section 5.2 show significant differences in propagation losses, likely caused by a difference in TiO_2 crystal phase. This could be caused by either of two differences in their processing steps: The deposition process time or the etching process time. Both of these processes heat up the sample, which could cause the formation of anatase phase TiO_2 [36]. To determine which of the two processes causes the formation of anatase phase TiO_2 , four samples were fabricated, in order to have all four combinations of thick and thin layers, and shallow and deep etches. The different process parameters, and resulting dimensions for all four samples are shown in Table 5.3.

Table 5.3: Fabrication parameters and dimensions for four samples, used to compare the impact of the deposition and etching times on propagation losses of the resulting waveguides.

Sample	Deposition time (min)	Etch time (min)	TiO_2 layer thickness (nm)	Expected etch depth (nm)
Thin shallow	45	1:30	83	80
Thin deep	45	6:00	83	400
Thick shallow	255	1:30	417	80
Thick deep	255	6:00	417	400

5.3.1 TiO_2 morphology

Using the setup explained in Section 5.1.2, the crystal phases present in each of the four samples were determined from the Raman spectra. The spectra for each sample can be seen in Fig. 5.8.

All four Raman spectra show the two silicon peaks at 521 cm^{-1} and 950 cm^{-1} , as expected. The peaks of interest are the peaks that were already seen in the measurement in Fig. 5.4 at 384 cm^{-1} and 643 cm^{-1} . Both these peaks show up in both thick samples. The most prominent peak at 643 cm^{-1} seems to have the same shape for both the ‘thick, deep’, and the ‘thick, shallow’ sample. They are not visible in the spectra of the thin samples. This shows that the thin samples contain only amorphous TiO_2 , while the thick samples contain at least some anatase TiO_2 .

Compared to the measurement in Fig. 5.4, each peak in the spectrum is broader. This is caused by a bigger monochromator input slit width used, reducing its resolution.

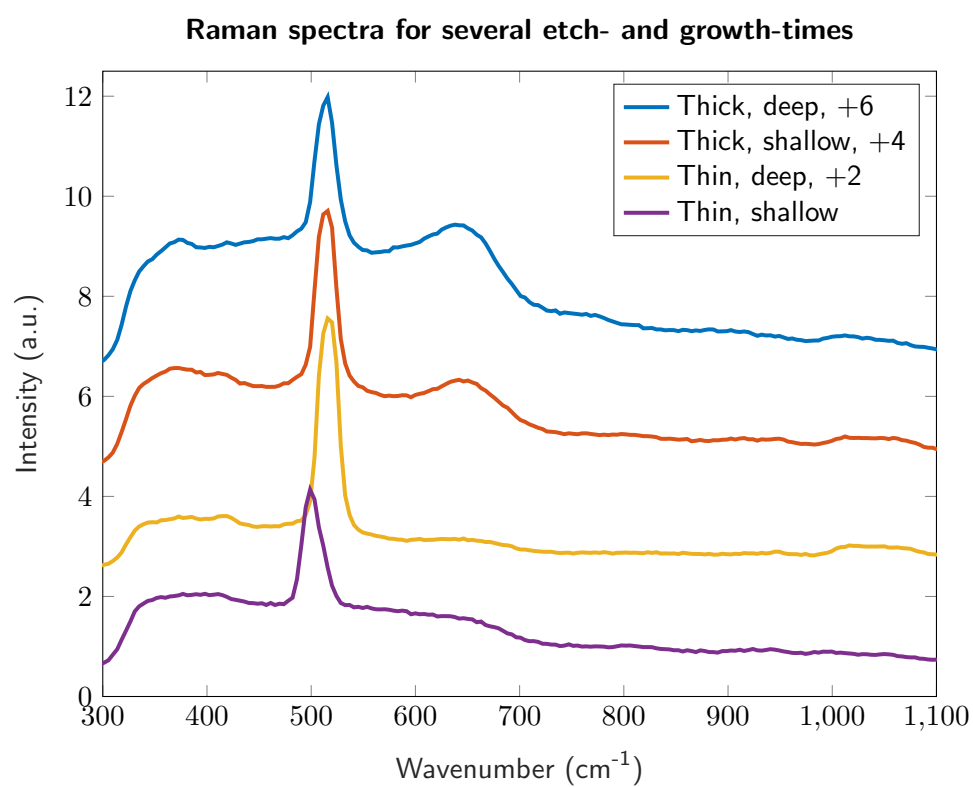


Figure 5.8: Raman spectra of 4 waveguides, with differing layer thickness and etch depths. Each spectrum has been offset for visibility.

5.3.2 Propagation loss measurements

Propagation loss measurements could be done on three of the four samples. The measurement could not be done on the 'Thick, shallow' sample, due to not being able to couple to the mode of the ridge waveguide; All light coupled into the sample was coupled into the slab mode, and did not follow the path of the waveguide. The measurement for the 'Thick, deep' sample could only be performed at a wavelength of 785 nm, since the losses were so high at 633 nm that the light did not reach to the spiral section. The propagation losses are shown in Table 5.4.

Table 5.4: Propagation losses of 4 waveguide samples, for 633 and 785 nm light.

Sample	TiO ₂ layer thickness (nm)	Etch depth (nm)	Propagation loss @633 nm (dB/cm)	Propagation loss @785 nm (dB/cm)
Thin shallow	83	80	8.2	12.9
Thin deep	83	400	50.0	10.0
Thick shallow	450	80	X	X
Thick deep	450	400	X	33.9

5.3.3 Discussion

From the Raman spectra of all four waveguide samples it is clear that the deposition process length has an impact on the morphology of the waveguides, while the length of the etching step has no effect on the morphology. The propagation loss measurements on the samples suggest the same, since the 'thick, deep' sample has the highest propagation losses at 785 nm, while the expected amount of losses assuming the same TiO₂ morphology would be similar to the thin samples.

5.4 Propagation loss reduction by modified sputtering process

In order to try to reduce the losses in the thick waveguide, a new fabrication run was started. The deposition process was slightly modified, to reduce the maximum temperature of the wafer during the process. This might lead to less crystallization in the layer. The propagation losses and Raman spectrum of the waveguides fabricated in this run were also characterized.

5.4.1 Sputtering process modification

To try to reduce the maximum temperature of the wafer during the deposition of a layer of 360 nm, the deposition was split into 6 steps, each lasting a maximum of 45 minutes. The sample was unloaded from the sputter machine between deposition steps, and the machine was cooled back to room temperature between every step. In this way, the

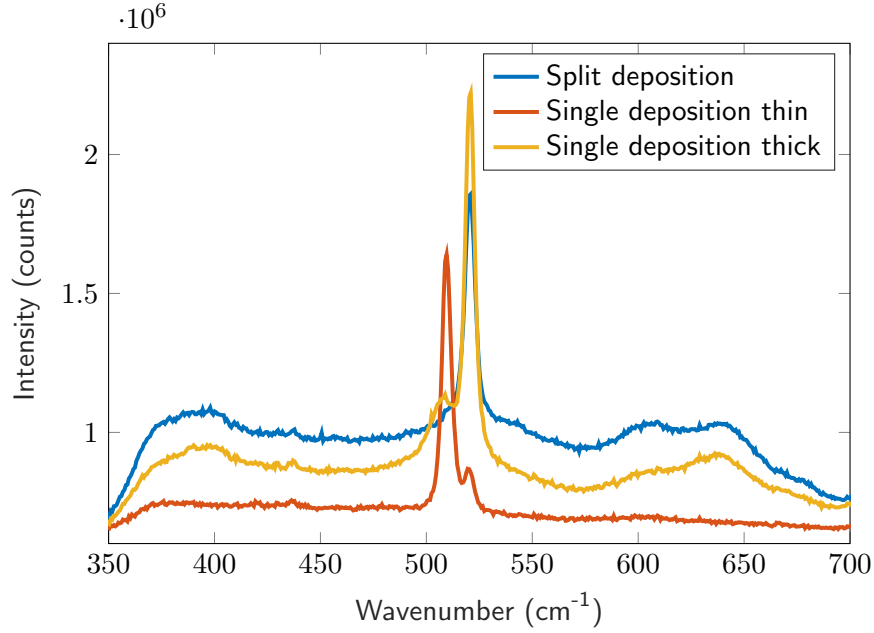


Figure 5.9: Raman spectrum of three waveguides, one fabricated using the modified, split deposition process, and two using the unmodified process, using a single deposition.

temperature of the wafer during deposition was expected to never raise above 34 °C, the maximum deposition temperature reached by the 74 nm amorphous layer.

For this particular fabrication run, the deposition was done in 5 steps of 45 minutes, followed by a step of 30 minutes. The resulting wafer had a TiO₂ layer of 460 nm in the center of the wafer, and 360 nm at the location where the waveguides are etched, 3 cm from the center.

5.4.2 Raman spectrum

The Raman spectrum for the new waveguide has been measured and is shown in Fig. 5.9. The measurement setup was improved, and the slit size on the monochromator reduced in between the measurements in Fig. 5.8 and Fig. 5.9. This leads to a higher wavenumber-resolution, therefore, the samples from Section 5.3.1 with a deep etch were measured again for comparison.

From this figure, it can be seen that the split deposition has no different peaks compared to the thick waveguide fabricated using a single deposition. Based on the broad peaks at 384 cm⁻¹ and 643 cm⁻¹ both these waveguides are expected to contain a mix of anatase- and amorphous TiO₂. A small peak that did not show up in previous measurements, due to the lower resolution, is the peak at 612 cm⁻¹. This peak is present in the Raman spectrum of rutile TiO₂ [30]. Therefore, some part of the TiO₂ is likely of the rutile phase as well.

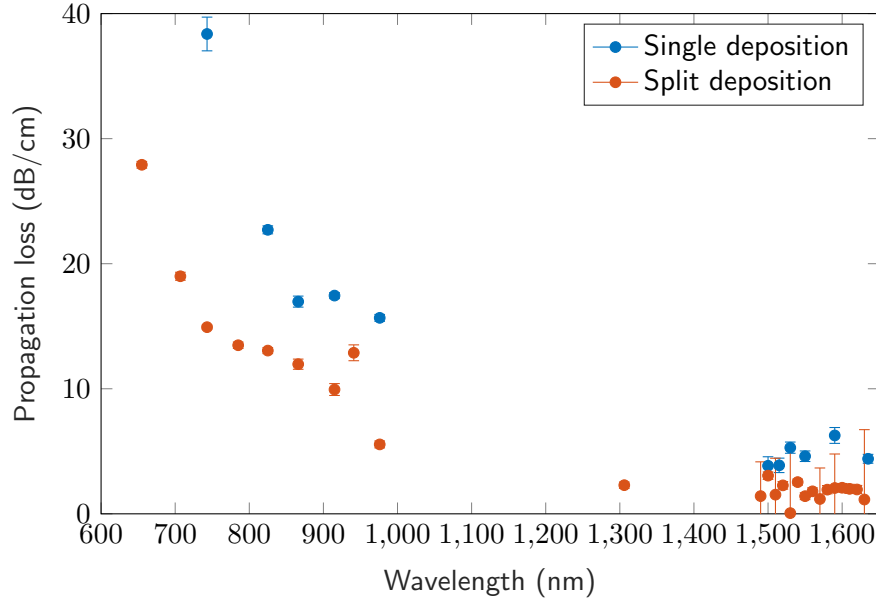


Figure 5.10: Loss at several wavelengths for two waveguides of 360 nm thickness. One waveguide is from a TiO_2 layers sputtered in one deposition run, while the other one had the deposition process split into 6 short depositions.

What becomes apparent for the single deposition waveguide samples from the new measurement is that there are two peaks, that were previously measured as a single peak: A silicon-peak at the expected place of 519.5 cm^{-1} , and a second peak at 509.6 cm^{-1} . The source of the 509.6 cm^{-1} peak is not known for sure. It could be caused by a silicon peak which is shifted due to tensile strain [38]. This seems unlikely though, since any strain that would build up in the layer stack during the TiO_2 growth is likely dissipated in the $8\text{ }\mu\text{m}$ SiO_2 layer, and not in the crystalline silicon substrate, which causes the narrow peak. The strain could have been caused by something different from the TiO_2 growth as well.

5.4.3 Propagation loss measurements

The propagation losses were measured for the new waveguides at several wavelengths, using three separate lasers: A Ti:Sapphire laser from 702 nm to 976 nm, a HP81552SM at 1306 nm, and an Agilent 81600B for the wavelengths of 1465 nm to 1635 nm to cover a wide wavelength range from 655 nm to 1635 nm. To be able to see whether the modified deposition process made a difference, the propagation losses of the 360 nm thick waveguide measured in Section 5.2 were also measured with two of the three lasers, to cover the same range. These results are shown in Fig. 5.10

The figure shows that the split deposition has lower losses at every measured wavelength. The general trend of the losses is similar for both waveguides.

5.4.4 Discussion

Even though the Raman spectra show no significant differences between the two deposition processes, the propagation losses between both waveguides are significantly different. This could be caused by differences in the layer that are not measured in the Raman-spectrum. The grain size between the sample could be different, or the ratio between amorphous and polycrystalline TiO_2 could be different. These differences are not easily recognized from the waveguide-Raman spectrum or an AFM scan. To check this hypothesis, a TEM image could be made of both samples. This would show the structure of the sample on an atomic level. It would also be able to tell if the crystallization happens throughout the entire layer, or only above certain critical thickness.

The data does make clear that the growth of or the conversion to polycrystalline anatase phase is not caused solely by the temperature during the deposition. It is also dependent on the thickness of the TiO_2 layer. This has also been demonstrated by H. W. Pan et al. in [37]. They had shown that for TiO_2 layers with different thicknesses sandwiched between SiO_2 layers the crystallization temperature is different. Thick layers were shown to crystallize at lower temperatures compared thinner layers. This is likely due to thermodynamics, where crystallization would need a bigger 'push' of energy to occur in thinner layers compared to thick ones, due to balances between volume energies and surface energies being different.

5.5 Summary and conclusion

In this chapter, several waveguides have been fabricated. The first waveguide sample was used to test whether OH groups were part of the layer, and whether the Ti in the layer was completely oxidized. Using FTIR, it was measured that OH groups were not present in the layers, but HTiO molecules were. The amount of HTiO molecules could not be quantified using this measurement. From XPS measurements, all Ti in the layer seems fully oxidized, which contradicts the FTIR measurement. It might be because the XPS measurement cannot discern between TiO_2 and HTiO. The XPS measurement did not measure any Ti in metallic form. Therefore, there will not be any metal absorption in the waveguides from these layers.

Additionally, propagation losses and Raman spectra of several waveguides have been measured. It is concluded that the waveguides with a thickness below 80 nm were completely amorphous, while waveguides thicker than 360 nm contained polycrystalline anatase and rutile form TiO_2 as well. The propagation losses for the amorphous 74 nm thick waveguide were measured to be 8.2 dB/cm at a wavelength of 785 nm. The best losses measured for thicker, partly polycrystalline waveguides at the same wavelength of 785 nm were 13.4 dB/cm for a waveguide of 360 nm thickness. Comparison of the mode overlaps with expected lossy regions in the waveguide would predict the losses to be the same between the waveguides. This shows that the morphology of the TiO_2 has an impact on the propagation losses of waveguides that are made of it, where the polycrystalline phase of TiO_2 causes higher losses compared to the amor-

phous phase of TiO. This is attributed to volume scattering losses in the polycrystalline waveguide.

The 360 nm waveguide with the lowest measured propagation losses has propagation losses at a 1310 nm wavelength of 2.20 ± 0.25 dB/cm, and at 1550 nm, they are 1.7 ± 1.6 dB/cm. This waveguide was fabricated using the modified sputtering process from Section 5.4. Compared to the waveguides made with the unmodified sputtering process from [23], the propagation losses were lower at every measured wavelength. Therefore, it can be concluded the modified sputtering process proposed in 5.4 should be used instead of the original process from [23] if low propagation losses are desired in a TiO₂ waveguide.

Chapter 6

Nonlinear measurement

The main goal of this thesis was to measure the nonlinear refractive index of the fabricated TiO_2 . A four wave mixing experiment is used for this measurement. This chapter starts with a description of the measurement setup used. After that, an analysis is made of the dispersion curves of the fabricated waveguides, and possible wavelengths for the measurement are determined. The actual measurement is first performed at a wavelength of 1300 nm, followed by a measurement at 980 nm.

6.1 Four wave mixing measurement setup

In order to measure four wave mixing, the pump and probe beam have to be combined into a single beam. This beam needs to be coupled to the sample, and the optical spectrum at the output of the sample has to be measured. The setup is schematically shown in Fig. 6.1

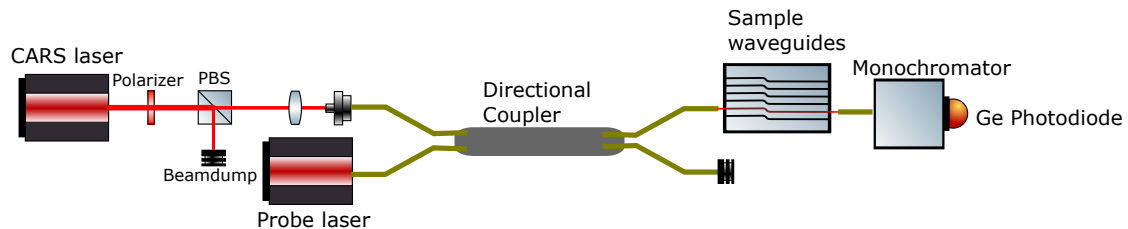


Figure 6.1: Measurement setup for measuring FWM.

6.1.1 Combining pump and probe beams

To keep the setup versatile, we chose to connect the entire setup using optical fibers, instead of using free-space light beams. This makes it very easy to swap components in the system. The disadvantage of using fibers is that nonlinear effects will play a role in those fibers [39], as well as in the sample. This reduces the detection limits of the setup.

To combine two fiber coupled beams, a directional coupler can be used. This is a fiber-based device with two input- and two output-ports. Light that enters one input port is divided over both output ports in the coupler-ratio, which is one of the coupler's specifications.

Using a directional coupler over free space optics has two disadvantages: Firstly, the coupler has an inherent power penalty, because the light from one input is split over two outputs instead of one. Secondly, directional couplers have a limited bandwidth, meaning the directional coupler needs to be swapped if the measurement wavelength changes.

An advantage of using the directional coupler over free space optics is that the second output port of the coupler can be used to monitor the spectrum and power coupled into the waveguide at the same time as measuring the output spectrum of the waveguide.

6.1.2 Spectrum measurement

For the measurement of the spectra at the input and output of the waveguide, an old monochromator was used. Using the smallest possible slit width of the monochromator, a linewidth of 0.5 nm is achieved.

The monochromator grating position could be controlled manually or electronically. For the manual control, the grating could be rotated with a crank. This same crank could also be turned by the built in stepper motor, with a resolution of 0.2 nm. In order to automate the spectrum-measurement, an Arduino was combined with 4 MOSFETs to drive the stepper motor. The stepper motor could then be rotated a given number of steps by sending commands to the Arduino over a serial port.

On the output of the monochromator, a germanium photodetector was mounted. A germanium detector was chosen because it is sensitive to light between 900 nm and 1600 nm [40], covering each of the three wavelengths considered during the design of the waveguides. The photodetector was connected to a DAQ through a transimpedance amplifier. The DAQ could be read out using Labview on a computer.

By combining the readout of the photodetector with the control of the stepper motor in a single Labview virtual instrument, the spectrum measurement was automated.

6.2 Dispersion analysis of fabricated waveguides

The dispersion of the waveguides that were fabricated with the modified sputter process was simulated using Lumerical MODE. These were the same waveguides as used for the loss measurements in Fig. 5.10, except for the differing width. Of these waveguides, the available waveguide widths that were fabricated were from 600 nm to 1400 nm, with steps of 100 nm. The simulated waveguide dispersions for the four narrowest waveguides are shown in Fig. 6.2. The dispersion for the wider waveguides is below -250 ps/nm/km for all wavelengths.

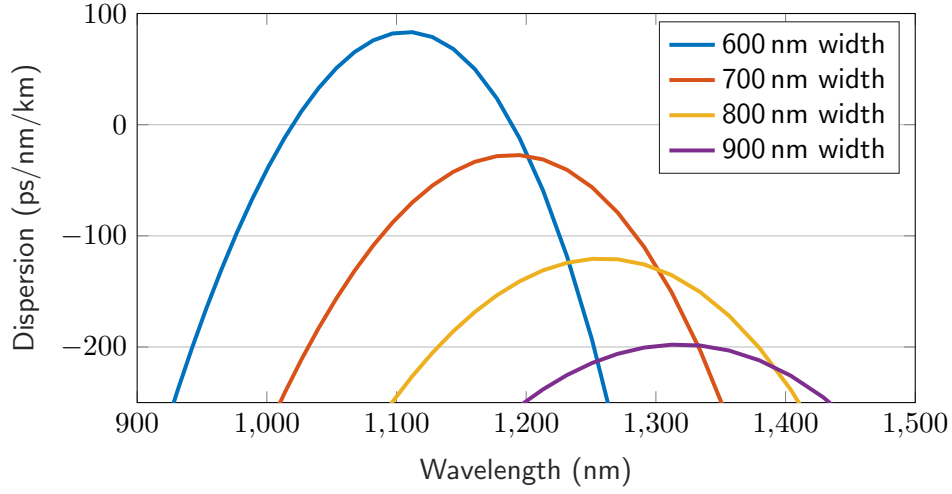


Figure 6.2: The simulated dispersion curves for fabricated 360 nm thick waveguides of different widths.

The figure shows that there is a zero-dispersion point at a wavelength of 1000 nm for the narrowest 600 nm waveguide. The same waveguide has a dispersion of -85 ps/nm/km at a wavelength of 980 nm. Therefore, the 600 nm wide waveguide should have the highest FWM efficiency at 980 nm. For 1300 nm, no zero-dispersion point was achieved in any of the waveguides, even though this was expected from the initial simulations shown in Fig. 3.2. The difference between the simulations is that the fabricated waveguides have a sidewall angle of 85° , instead of 90° . Looking at the trends in Fig. 3.2, it can be concluded that the fabricated waveguides are too thin for a zero-dispersion point at 1300 nm. The lowest amount of dispersion achieved at 1300 nm wavelengths is for the 800 nm wide waveguides. These have a dispersion of -135 ps/nm/km at 1300 nm. Filling these values into equation 2.17 leads to a phase mismatch $\Delta k = 4.6 \times 10^{-4} \text{ m}^{-1}$ for a wavelength spacing of 2 nm, or $\Delta k = 2.9 \times 10^{-3} \text{ m}^{-1}$ for a wavelength spacing of 5 nm. This leads to coherence lengths $\frac{2\pi}{\Delta k}$ of 13.6 km and 2.2 km respectively. Therefore, the FWM process should still be phase matched well enough that for a propagation distance on the order of centimetres, the phase mismatch will be negligible.

It can also be seen that for the narrowest 600 nm waveguide, there is a wavelength range where the dispersion is higher than 0 ps/nm/km , which is also called anomalous dispersion [6]. This gives the possibilities for solitons to be generated in the waveguide [41].

6.3 FWM measurement at 1300 nm

The initial expectation before fabricating the waveguides was that efficient FWM would be possible with 1310 nm light, so a setup had already been built for measurement near this wavelength. After building the setup, it became clear that approximately 1000 nm

light would generate FWM more efficiently. Therefore, the first measurements were done using light near 1310 nm. The used pump- and probe-laser are described in the following section, followed by the measurement results and discussion of the results.

6.3.1 Pump laser

The most important component in a setup for measuring FWM is a laser source with intensities that are high enough to generate detectable FWM in the sample waveguides. One powerful laser system available in the Optical Sciences group is the one used for the CARS microscope setup. This system has the added benefit of being tunable across a wide range of wavelengths as well, since it uses an Optical Parametric Oscillator (OPO) for frequency conversion of the light. This system supports wavelengths near 1310 nm.

The following OPO settings were found to output a single wavelength peak around 1310 nm: Piezo position: 2135, Crystal temperature: 162 °C. Since the Lyott filter cannot be read out, it was tuned to the position where maximum power output was observed. This resulted in an output beam with a wavelength of 1300 nm

The CARS laser system generates a pulsed laser beam. The repetition rate is 80 MHz, with a pulse length of 5 ps, giving a duty cycle of 0.4%. The average power output by the system is up to 10 W, which would lead to peak powers of $\frac{10}{0.004} = 2.5$ kW, if a square pulse shape is assumed. Since the actual pulse shape is smoother than a square shape, the actual peak power is likely even higher. On the other hand, the pulse transport in the fiber will broaden the pulse shape due to dispersion, therefore lowering the peak power.

The laser system is a free space system, and not a fiber coupled one. Before coupling the beam into a fiber, it was passed through a polarizer and polarizing beam splitter. This gives the ability to change the power coupled into the fiber by rotating the polarizer. After the polarizing beam splitter, the beam was focused on a SMF-28 fiber facet using an objective. This fiber transported the light to the optical table where the measurement was done.

6.3.2 Probe laser

The second important component necessary for FWM to occur is the probe laser. The intensity of this beam is less important compared to the pump, since the amount of FWM occurring will scale proportionally to the probe-beam power, while it scales quadratically with the pump-beam power as shown in Section 2.2.5. For the probe beam, the most abundant laser in the lab was used: The HP81552SM Fabry-Perot laser, mounted in a Lightwave Multimeter. This is a continuous wave laser source, with a maximum output power of 1 mW

6.3.3 Measurement results

For the measurement at 1300 nm, a waveguide with a single S-bend was used. The total propagation length is 1.2 cm. The in- and out-coupling from the waveguides to

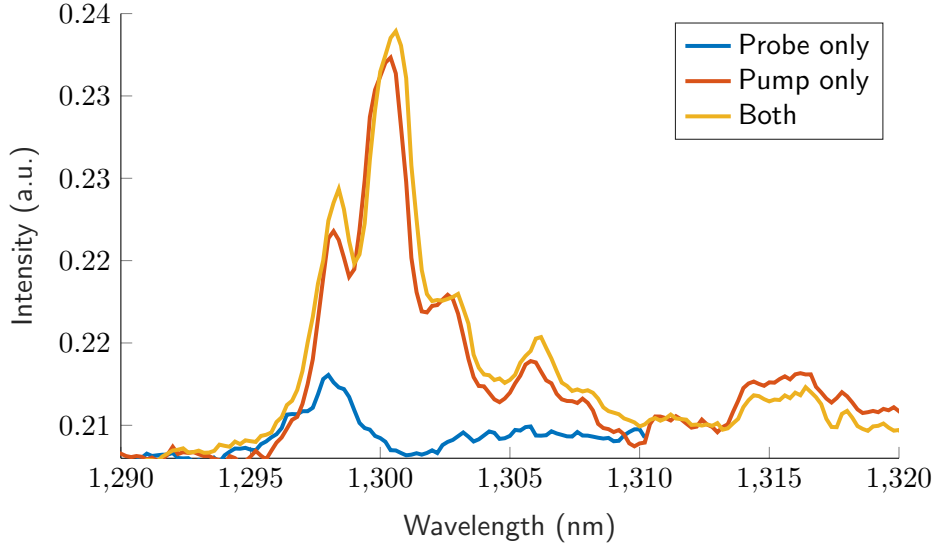


Figure 6.3: Four wave mixing results at 1300 nm. The probe beam power in the waveguide is $6.3 \mu\text{W}$ CW. The pump beam power in the waveguide is $19 \mu\text{W}$ time averaged, or 4.8 mW peak.

the fibers was done using bare fiber coupling. The total loss between the input- and output fiber was 50 dB. This was expected to be caused by 2 dB propagation losses, and two times 24 dB fiber coupling losses. From the lasers to the sample fiber, there's another 3 dB of losses in the directional coupler.

With the pump laser turned off, the amount of probe laser-power that was transmitted through the entire setup was measured to be 2 nW. Once corrected for 24 dB waveguide to fiber-coupling losses, the amount of probe laser power that propagated through the waveguide was only $6.3 \mu\text{W}$.

The power of the probe laser was not directly measurable, since the used power-meter could not measure pulsed sources. The spectrum analyzer measured its average power to be 3 times higher than the probe source, giving a time averaged power of $19 \mu\text{W}$ in the waveguide, or a peak power of 4.8 mW .

Three spectra were measured: With both lasers turned on, with only the pump laser turned on, and with only the probe laser turned on. The spectra were all measured at the output end of the waveguide. The spectra are plotted in Fig. 6.3.

As can be seen from the figure, no extra wavelengths were generated in the waveguide with both lasers turned on using these laser powers. However, There are four wavelength peaks in the pump laser beam's spectrum. The spectrum for the pump laser had the same peaks when it was measured before propagating through the waveguide. Therefore, these frequencies were not generated via spontaneous FWM in the waveguide. It is not known whether these four peaks are also in the original laser beam, or if they were generated during propagation through the fiber and/or the directional coupler.

6.3.4 Discussion

The fact that no FWM occurred in the waveguide in our measurement is not surprising. The powers that were achieved inside the waveguide were not high enough to generate a detectable signal. From the propagation losses of 2.2 dB/cm and the propagation length of 1.2 cm, an effective length of 0.9 cm is calculated. If the highest nonlinear parameter as achieved in [22] is assumed, equation 2.22 can be used to calculate the conversion efficiency of the waveguides at the peak power of the pulse:

$$CE = (L_{\text{eff}} P_{\omega_1} \gamma)^2 = 0.9 \text{ cm} \times 4.8 \text{ mW} \times 34 \text{ W}^{-1} \text{ m}^{-1} = 1.47 \times 10^{-3} = -28 \text{ dB} \quad (6.1)$$

This signal is only generated 0.4% of the time, therefore, the measured signal will be only $-28 \text{ dB} \times 0.004 = -52 \text{ dB}$. It can be seen from Fig. 6.3 that a signal 52 dB lower than the probe signal would be below the detection limit of the used spectrometer. This would be a signal with a power of -108 dBm .

In the waveguides used by Guan et al. in [22], the lowest laser powers where measureable four wave mixing was achieved was with a pump power of 25 mW and a probe power of 3 mW coupled into the waveguide. This resulted in the generation of a new wavelength of light with a power 46 dB lower than that of the probe beam, over an interaction length of 1.1 c/metre. The waveguide used in those measurements is very similar to our waveguide, and therefore it is expected similar powers are necessary in our waveguides to generate a measureable amount of FWM.

In the setup used for the measurement at 1300 nm, the largest power loss is caused by the coupling between the fibers and the waveguide. The simulated mode overlap between the first order modes of the waveguide and the fiber at 1300 nm is only 2%. Therefore, the maximum coupling efficiency that can be reached using direct fiber to waveguide coupling is -17 dB . Guan et al. reached coupling efficiencies of -7 dB in [22] by using tapered and lensed fibers, instead of standard fibers.

6.4 FWM measurement at 980 nm

From the FWM measurement at 1300 nm it is clear the used laser powers were not high enough to induce FWM. Therefore, the measurement setup was modified, to allow a measurement at 980 nm.

6.4.1 Pump laser

For the pump laser, a diode laser at a wavelength of 980 nm is used. It has a maximum output power of 400 mW CW. After accounting for 3 dB loss in the directional coupler, the remaining power before fiber-to-waveguide coupling is 200 mW, which is 23 dBm.

6.4.2 Probe laser

For the probe laser, a Ti:Sapphire laser is used. The wavelength of the laser is tuned to 976.7 nm. The available power after laser-to-fiber coupling is 200 mW. Accounting for the 3 dB loss in the directional coupler leaves 100 mW of power before the fiber-to-waveguide coupling, which is equal to 20 dBm.

6.4.3 Fiber to waveguide coupling

The laser powers coupled into the waveguide reached by Guan et al. in [22] were pump and probe powers of 25 mW and 3 mW respectively. This is equal to powers of 14 dBm and 4.7 dBm respectively. As was shown in Section 2.2.5, the four wave mixing efficiency scales with the pump laser power P_{pump} and probe laser power P_{probe} as $P_{\text{pump}}^2 P_{\text{probe}}$. the value of P_{probe} as $P_{\text{pump}}^2 P_{\text{probe}}$ is equal to 32.7 dBm in the minimum power case shown in [22]. For our measurement, this value will be equal to $66 - 3L_{\text{coupling}}$ dBm, where L_{coupling} is the coupling loss in dB. Therefore, similar FWM efficiency as in [22] could be achieved if $L_{\text{coupling}} = \frac{66-32.7}{3} = 11.1$ dB, assuming that the nonlinear parameter of our waveguides is similar to theirs. Likely, the nonlinear parameter in our measurement will be higher, since the waveguide is smaller, leading to a smaller effective mode area. Also, the nonlinear parameter is higher when a shorter wavelength of light is used, since the value for k_0 in equation 2.20 will increase for shorter wavelengths.

Using a tapered and lensed fiber, this coupling loss is possible, as coupling losses of only 7 dB were achieved in the same way in [22]. Therefore, fiber-to-waveguide coupling using a tapered and lensed fiber was chosen for the measurement.

6.4.4 Measurement results

The measurement using the proposed setup has not yet been carried out.

Chapter 7

Summary and conclusions

In this thesis, TiO₂ waveguides have been designed and fabricated, which can be used to measure FWM in TiO₂. The losses of the waveguides have been measured, and a FWM experiment was carried out. A short summary of the thesis is given, and where possible, conclusions are drawn.

7.1 Zero-dispersion waveguide fabrication

In Chapter 3 the dispersion of TiO₂ waveguides on an SiO₂ substrate has been simulated for waveguide widths from 0.7 μm to 1.2 μm and for thicknesses between 300 nm and 460 nm. Within these limits, waveguides with zero dispersion are possible for the wavelengths of 1310 nm and 1550 nm, as well as other wavelengths. Within these limits, no waveguide can be made with zero dispersion for 1000 nm light.

After developing the fabrication process in Chapter 4, the actual dimension possibilities for fabrication turned out to be smaller than expected. The maximum waveguide thickness that can be fabricated is approximately 400 nm. The minimum waveguide width that can be fabricated is 0.6 μm . Therefore, one set of waveguides has been fabricated with zero dispersion at a wavelength of 1000 nm. These waveguides have a thickness of 360 nm and a width of 0.6 μm . Another set of waveguides with a dispersion of $-135 \text{ ps}/\text{nm}/\text{km}$ at 1300 nm has also been fabricated. These waveguides have a thickness of 360 nm, and a width of 0.8 μm .

7.2 Waveguide propagation losses

In Chapter 5, the propagation losses of fabricated TiO₂ waveguides have been measured. In 360 nm thick waveguides with a width of 1.2 μm , the propagation losses measured at 1310 nm were $2.20 \pm 0.25 \text{ dB}/\text{cm}$, and at 785 nm the losses were 13.4 dB/cm. A fabricated 74 nm thick waveguide of the same width had propagation losses of 8.2 dB/cm, even though the theory predicts losses equal to the 360 nm thick waveguide. The difference between the propagation losses was attributed to the difference in morphology

between both waveguides. The 74 nm thick waveguide consisted of amorphous TiO_2 , while the thicker 360 nm waveguide consisted of a mix of amorphous and polycrystalline anatase TiO_2 . The grain boundaries in the polycrystalline material cause extra volume scattering losses which do not occur in the waveguide of amorphous TiO_2 .

7.3 FWM measurement

In Chapter 6, a FWM measurement was carried out for a wavelength of 1300 nm, with waveguides of 360 nm thickness with a width of 0.8 μm . No FWM was detected. This was correct with the expectations, since the laser powers that could be coupled to the waveguide were too low to generate detectable FWM.

A setup has been proposed to do the FWM measurement at a wavelength of 980 nm, where the achieved powers are likely high enough. The measurement has not been carried out at this wavelength yet.

Chapter 8

Outlook

One of the reasons TiO_2 is a promising waveguide material is the wide transparency window combined with the high nonlinear refractive index. If rare earth dopants are introduced in the layer, optical gain can be achieved in the material. If the reached intensities are high enough, the nonlinearity of the TiO_2 could be used to convert the fixed wavelengths from the gain material to different wavelengths. This gives the opportunity to make on-chip laser sources capable of outputting a wide range of wavelengths, including the visible range.

In order to be able to efficiently convert the wavelength generated from the rare earth doping, phase matching has to be achieved at the wavelength of interest. From the simulations, this does not seem possible with 80 nm thick waveguides. As can be seen from Fig. 3.1, the dispersion decreases for decreasing waveguide thicknesses. Therefore, to be able to make the wavelength conversion work in the visible, the layer needs to be grown thicker. This is not possible using the current process without converting the TiO_2 into polycrystalline anatase phase, and therefore without increasing the propagation losses in the visible range. Increased propagation losses would of course reduce the efficiency of the laser system. Therefore, a process is desired that can grow ± 360 nm TiO_2 layers of a non-polycrystalline phase. This leaves the possibilities of growing a thick amorphous layer, or a thick monocrystalline layer.

8.1 TiO_2 layer growth

From the analyses of the crystal structures of several waveguides, it was concluded that the fabricated waveguides thicker than 360 nm were of polycrystalline material, while waveguides of 80 nm thickness or lower were amorphous. Consequently, the thicker waveguides had higher propagation losses, especially in the visible wavelengths.

8.1.1 Amorphous growth

Using the reactive sputtering process, it is possible to grow amorphous layers, as was demonstrated in the layers characterized below 80 nm thickness. If more research is

done regarding the crystallization mechanisms and for which conditions they occur, it might be possible that a modified sputtering process could grow amorphous layers of the desired thickness. Of course, the addition of rare earth dopants will change growth conditions as well, which might increase or decrease the possible amorphous layer thickness.

The substrate that the TiO_2 is grown on likely plays a role as well, since it will have a big effect on the growth conditions of the first few atomic layers of TiO_2 . These effects then propagate up through the layer during growth. Effects of strain in the layers could also play a role, since it seems the 74 nm layer measured in Fig. 5.9 has stress in the Si substrate. Maybe thicker amorphous layers can be grown if the stress is reduced, by choosing a different substrate for the TiO_2 layer.

8.1.2 Monocrystalline growth

The other promising way to grow TiO_2 is using single-domain epitaxy, to grow monocrystalline layers. In literature, the (110) rutile phase of TiO_2 has been grown on both (110) MgF substrates with a thickness of around 200 nm [42] and on (100) Ge substrates with a thickness of 30 nm [43]. Both of these publications used a PLD process. Epitaxial growth of full layers of anatase TiO_2 has not been found in literature. Of course, the growth possibilities could change once rare earth dopants are added to the material.

The added benefit of using the rutile phase of TiO_2 is that it has a higher refractive index compared to the layers used in this research. The refractive index at 633 nm is 2.58 and 2.87 for the ordinary and extra-ordinary directions respectively. This means the confinement of the mode in the waveguide is higher. This in turn causes a smaller mode area, and therefore more intense electric field strengths. This improves the efficiency of nonlinear processes.

8.2 Utilizing anomalous dispersion

Waveguides with anomalous dispersion from 1000 nm to 1200 nm have been fabricated. These waveguides could be used to generate solitons, or generate supercontinua [44]. If the dispersion is increased, the wavelength range where such effects would be achievable can be expanded as well.

Bibliography

- [1] B. Glover, *History of the atlantic cable and submarine telegraphy - cable timeline*. [Online]. Available: <http://atlantic-cable.com/Cables/CableTimeLine/index1951.htm>.
- [2] H. Ashiba, M. Fujimaki, K. Awazu, T. Tanaka, and M. Makishima, "Microfluidic chips for forward blood typing performed with a multichannel waveguide-mode sensor," *Sensing and Bio-Sensing Research*, vol. 7, pp. 121–126, 2016, ISSN: 2214-1804. DOI: <https://doi.org/10.1016/j.sbsr.2016.01.012>. [Online]. Available: <http://www.sciencedirect.com/science/article/pii/S2214180416300125>.
- [3] P. A. Franken, A. E. Hill, C. W. Peters, and G. Weinreich, "Generation of optical harmonics," *Phys. Rev. Lett.*, vol. 7, pp. 118–119, 4 Aug. 1961. DOI: 10.1103/PhysRevLett.7.118. [Online]. Available: <https://link.aps.org/doi/10.1103/PhysRevLett.7.118>.
- [4] *Nonlinear effect*. [Online]. Available: http://support.huawei.com/online/toolsweb/resources/en/21_nonlinear.html.
- [5] M. Nkzawa, K. Suzuki, E. Yamada, H. Kubota, Y. Kimura, and M. Takaya, "Experimental demonstration of soliton data transmission over unlimited distances with soliton control in time and frequency domains," *Electronics Letters*, vol. 29, no. 9, pp. 729–730, Apr. 1993, ISSN: 0013-5194.
- [6] R. W. Boyd, *Nonlinear Optics*. Academic Press, 2008, ISBN: 0123694701.
- [7] C. G. H. Roeloffzen, M. Hoekman, E. J. Klein, L. S. Wevers, R. Timens, D. Marchenko, D. Gekus, R. Dekker, A. Alippi, R. Grootjans, A. Rees, R. M. Oldenbeuving, J. Epping, R. Heideman, K. Worhoff, A. Leinse, D. Geuzebroek, E. Schreuder, P. W. L. Van Dijk, and K. Boller, "Low loss si3n4 triplex optical waveguides: Technology and applications overview," vol. PP, pp. 1–1, Jan. 2018.
- [8] H. H. Li, "Refractive index of silicon and germanium and its wavelength and temperature derivatives," *Journal of Physical and Chemical Reference Data*, vol. 9, no. 3, pp. 561–658, 1980. DOI: 10.1063/1.555624. eprint: <https://doi.org/10.1063/1.555624>. [Online]. Available: <https://doi.org/10.1063/1.555624>.

- [9] C. S. Wong, T. K. Liang, M. W. K. Mak, H. K. Tsang, I. E. Day, A. Harpin, J. Drake, and M. Asghari, "Measurement of nonlinear optical properties of silicon waveguide at 1.55 μm wavelength," in *Technical Digest. Summaries of papers presented at the Conference on Lasers and Electro-Optics. Postconference Technical Digest (IEEE Cat. No.01CH37170)*, May 2001, pp. 178–. DOI: 10.1109/CLEO.2001.947677.
- [10] J. Kischkat, S. Peters, B. Gruska, M. Semtsiv, M. Chashnikova, M. Klinkmüller, O. Fedosenko, S. Machulik, A. Aleksandrova, G. Monastyrskyi, Y. Flores, and W. T. Masselink, "Mid-infrared optical properties of thin films of aluminum oxide, titanium dioxide, silicon dioxide, aluminum nitride, and silicon nitride," *Appl. Opt.*, vol. 51, no. 28, pp. 6789–6798, Oct. 2012. DOI: 10.1364/AO.51.006789. [Online]. Available: <http://ao.osa.org/abstract.cfm?URI=ao-51-28-6789>.
- [11] R. Lahiri, A. Ghosh, S. M. M. D. Dwivedi, S. Chakrabartty, P. Chinnamuthu, and A. Mondal, "Performance of erbium-doped tio₂ thin film grown by physical vapor deposition technique," *Applied Physics A*, vol. 123, no. 9, p. 573, Aug. 2017, ISSN: 1432-0630. DOI: 10.1007/s00339-017-1180-2. [Online]. Available: <https://doi.org/10.1007/s00339-017-1180-2>.
- [12] V. Dimitrov and S. Sakka, "Linear and nonlinear optical properties of simple oxides. II," *J. Appl. Phys.*, vol. 79, no. 1996, p. 1741, 1996, ISSN: 00218979. DOI: 10.1063/1.360963. [Online]. Available: <http://scitation.aip.org/content/aip/journal/jap/79/3/10.1063/1.360963>.
- [13] K. Luke, Y. Okawachi, M. R. E. Lamont, A. L. Gaeta, and M. Lipson, "Broadband mid-infrared frequency comb generation in a si₃n₄ microresonator," *Opt. Lett.*, vol. 40, no. 21, pp. 4823–4826, Nov. 2015. DOI: 10.1364/OL.40.004823. [Online]. Available: <http://ol.osa.org/abstract.cfm?URI=ol-40-21-4823>.
- [14] C. J. Krückel, A. Fülöp, T. Klintberg, J. Bengtsson, P. A. Andrekson, and V. Torres-Company, "Linear and nonlinear characterization of low-stress high-confinement silicon-rich nitride waveguides," *Opt. Express*, vol. 23, no. 20, pp. 25 827–25 837, Oct. 2015. DOI: 10.1364/OE.23.025827. [Online]. Available: <http://www.opticsexpress.org/abstract.cfm?URI=oe-23-20-25827>.
- [15] S. Adachi, "Optical dispersion relations for gap, gaas, gasb, inp, inas, insb, alxga_{1-x}as, and in_{1-x}gaxasyp_{1-y}," *Journal of Applied Physics*, vol. 66, no. 12, pp. 6030–6040, 1989. DOI: 10.1063/1.343580. eprint: <https://doi.org/10.1063/1.343580>. [Online]. Available: <https://doi.org/10.1063/1.343580>.
- [16] S. M. Martinussen, R. N. Frentrop, M. Dijkstra, F. Segerink, V. Tormo-Márquez, J. Olivares, and S. García-Blanco, *Pedestal disk resonator in potassium yttrium double tungstate*, 2018. DOI: 10.1117/12.2289887. [Online]. Available: <https://doi.org/10.1117/12.2289887>.
- [17] R. G. Hunsperger, *Integrated Optics: theory and technology*. Springer, 2010.
- [18] M. Gottlieb, G. Brandt, and J. Conroy, "Out-of-plane scattering in optical waveguides," *IEEE Transactions on Circuits and Systems*, vol. 26, no. 12, pp. 1029–1035, Dec. 1979, ISSN: 0098-4094. DOI: 10.1109/TCS.1979.1084604.

- [19] R. Paschotta, *Group velocity dispersion*, Oct. 2017. [Online]. Available: https://www.rp-photonics.com/group_velocity_dispersion.html.
- [20] U. D. Dave, B. Kuyken, F. Leo, S.-P. Gorza, S. Combrie, A. D. Rossi, F. Raineri, and G. Roelkens, "Nonlinear properties of dispersion engineered ingap photonic wire waveguides in the telecommunication wavelength range," *Opt. Express*, vol. 23, no. 4, pp. 4650–4657, Feb. 2015. DOI: 10.1364/OE.23.004650. [Online]. Available: <http://www.opticsexpress.org/abstract.cfm?URI=oe-23-4-4650>.
- [21] J. Nowotny, *Oxide Semiconductors for Solar Energy Conversion: Titanium Dioxide (Green Chemistry and Chemical Engineering)*. CRC Press, 2011, ISBN: 1439848394. [Online]. Available: <https://www.amazon.com/Oxide-Semiconductors-Solar-Energy-Conversion/dp/1439848394?SubscriptionId=AKIAIOBINVZYXZQZ2U3A&tag=chimbiori05-20&linkCode=xm2&camp=2025&creative=165953&creativeASIN=1439848394>.
- [22] X. Guan, H. Hu, L. K. Oxenløwe, and L. H. Frandsen, "Compact titanium dioxide waveguides with high nonlinearity at telecommunication wavelengths," *Opt. Express*, vol. 26, no. 2, p. 1055, Jan. 2018, ISSN: 1094-4087. DOI: 10.1364/OE.26.001055. [Online]. Available: https://www.osapublishing.org/DirectPDFAccess/295B377C-C8CA-CDB1-758875BBCC1210A9%7B%5C_%7D380670/oe-26-2-1055.pdf?da=1%7B%5C&%7Ddid=380670%7B%5C&%7Dseq=0%7B%5C&%7Dmobile=no%20https://www.osapublishing.org/abstract.cfm?URI=oe-26-2-1055.
- [23] I. Hegeman, "TiO₂ waveguides for on-chip raman spectroscopy," Master's thesis, University of Twente, 2018.
- [24] J. D. B. Bradley, C. C. Evans, J. T. Choy, O. Reshef, P. B. Deotare, F. Parsy, K. C. Phillips, M. Lončar, and E. Mazur, "Submicrometer-wide amorphous and polycrystalline anatase TiO₂ waveguides for microphotonic devices," *Opt. Express*, vol. 20, no. 21, p. 23 821, 2012, ISSN: 1094-4087. DOI: 10.1364/OE.20.023821. [Online]. Available: <https://www.osapublishing.org/oe/abstract.cfm?uri=oe-20-21-23821>.
- [25] Moxfyre. (Sep. 2018). Energy-level diagram showing the states involved in raman spectra., [Online]. Available: https://en.wikipedia.org/wiki/Raman_spectroscopy#/media/File:Raman_energy_levels.svg.
- [26] J. H. Parker Jr., D. W. Feldman, and M. Ashkin, "Raman scattering by silicon and germanium," *Phys. Rev.*, vol. 155, no. 3, p. 712, 1967, ISSN: 0031899X. DOI: 10.1103/PhysRev.155.712. [Online]. Available: <http://link.aps.org/doi/10.1103/PhysRev.155.712>.
- [27] J. Park, S. K. Ozdemir, F. Monifi, T. Chadha, S. H. Huang, P. Biswas, and L. Yang, "Titanium Dioxide Whispering Gallery Microcavities," *Adv. Opt. Mater.*, vol. 2, no. 8, pp. 711–717, 2014, ISSN: 21951071. DOI: 10.1002/adom.201400107.
- [28] C. C. Evans, "Nonlinear optics in titanium dioxide : from bulk to integrated optical devices," PhD thesis, Harvard university, 2013. [Online]. Available: <http://nrs.harvard.edu/urn-3:HUL.InstRepos:11181139>.

- [29] C. C. Evans, C. Liu, and J. Suntivich, "Low-loss titanium dioxide waveguides and resonators using a dielectric lift-off fabrication process," *Opt. Express*, vol. 23, no. 9, p. 11 160, 2015, ISSN: 1094-4087. DOI: 10.1364/OE.23.011160. [Online]. Available: <https://www.osapublishing.org/abstract.cfm?URI=oe-23-9-11160>.
- [30] U. Balachandran and N. Eror, "Raman spectra of titanium dioxide," *J. Solid State Chem.*, vol. 42, no. 3, pp. 276–282, 1982, ISSN: 00224596. DOI: 10.1016/0022-4596(82)90006-8. [Online]. Available: <http://www.scopus.com/inward/record.url?eid=2-s2.0-0020130925%7B%5C%7DpartnerID=tZ0tx3y1>.
- [31] B. E. A. Saleh and M. C. Teich, *Fundamentals of photonics*, 2nd ed. Wiley-Interscience, 2009.
- [32] K. Worhoff, J. D. B. Bradley, F. Ay, D. Geskus, T. P. Blauwendraat, and M. Pollnau, "Reliable low-cost fabrication of low-loss $\text{Al}_2\text{O}_3:\text{Er}^{3+}$ waveguides with 5.4-dB optical gain," *IEEE Journal of Quantum Electronics*, vol. 45, no. 5, pp. 454–461, May 2009, ISSN: 0018-9197.
- [33] M. Zhou, L. Zhang, J. Dong, and Q. Qin, "Reactions of group iv metal atoms with water molecules. matrix isolation ftir and theoretical studies," *Journal of the American Chemical Society*, vol. 122, no. 43, pp. 10 680–10 688, 2000. DOI: 10.1021/ja0020658. eprint: <https://doi.org/10.1021/ja0020658>. [Online]. Available: <https://doi.org/10.1021/ja0020658>.
- [34] Shimanouchi and Takehiko, *Tables of molecular vibrational frequencies, consolidated volume i*. DOI: 10.6028/NBS.NSRDS.39. [Online]. Available: <https://nvlpubs.nist.gov/nistpubs/Legacy/NSRDS/nbsnsrds39.pdf>.
- [35] L. Nichtová, R. Kužel, and Z. Matěj, *Xrd study of thickness dependence of crystallization and stresses of TiO_2 thin films*. [Online]. Available: <http://www.xray.cz/xray/csca/kol2009/abst/nichtova.htm>.
- [36] G. Kaune, M. Rawolle, D. Magerl, and C. M. Papadakis, "Crystallization behavior of TiO_2 thin films," pp. 4–5,
- [37] H.-W. Pan, S.-J. Wang, L.-C. Kuo, S. Chao, M. Principe, I. M. Pinto, and R. De-Salvo, "Thickness-dependent crystallization on thermal anneal for titania/silica nm-layer composites deposited by ion beam sputter method," *Opt. Express*, vol. 22, no. 24, p. 29 847, 2014, ISSN: 1094-4087. DOI: 10.1364/OE.22.029847. [Online]. Available: <https://www.osapublishing.org/oe/abstract.cfm?uri=oe-22-24-29847>.
- [38] E. Anastassakis, A. Pinczuk, E. Burstein, F. H. Pollak, and M. Cardona, "Effect of static uniaxial stress on the Raman spectrum of silicon," *Solid State Commun.*, vol. 88, no. 11-12, pp. 1053–1058, 1993, ISSN: 00381098. DOI: 10.1016/0038-1098(93)90294-W.
- [39] G. Agrawal, *Nonlinear Fiber Optics (Fifth Edition)*, Fifth Edition, G. Agrawal, Ed., ser. Optics and Photonics. Boston: Academic Press, 2013, pp. 27–56. DOI: <https://doi.org/10.1016/B978-0-12-397023-7.00002-4>. [Online]. Available: <http://www.sciencedirect.com/science/article/pii/B9780123970237000024>.

- [40] H. Alexander, *Photodetectors test pulsed laser diodes*, Dec. 2002. [Online]. Available: https://www.photonics.com/Articles/Photodetectors_Test_Pulsed_Laser_Diodes/a14379.
- [41] R. Paschotta, *Solitons*, Jun. 2018. [Online]. Available: <https://www.rp-photonics.com/solitons.html>.
- [42] Y. Xie, L. Wei, Q. Li, Y. Chen, S. Yan, J. Jiao, G. Liu, and L. Mei, "Epitaxial rutile TiO₂ film based on MgF₂ substrate for ultraviolet detector," vol. 683, pp. 439–443, 2016. DOI: 10.1016/j.jallcom.2016.05.126.
- [43] Y. Suzuki, T. Nagata, Y. Yamashita, and T. Nabatame, "Thin-film growth of (110) rutile TiO₂ on (100) Ge substrate by pulsed laser deposition," vol. 06, pp. 1–5, 2016.
- [44] U. D. Dave, C. Ciret, S.-P. Gorza, S. Combrie, A. De Rossi, F. Raineri, G. Roelkens, and B. Kuyken, "Dispersive-wave-based octave-spanning supercontinuum generation in InGaP membrane waveguides on a silicon substrate," *Opt. Lett.*, vol. 40, no. 15, p. 3584, Aug. 2015, ISSN: 0146-9592. DOI: 10.1364/OL.40.003584. [Online]. Available: <https://www.osapublishing.org/abstract.cfm?URI=ol-40-15-3584>.

Appendix A

Process flow for waveguide fabrication

The process steps used to make the waveguides that were used for the FWM measurements are given below. The used wafer is a P-doped (100) Silicon wafer, with a 8 μm SiO_2 layer.

A.1 Wafer preparation

Measure oxide thickness

Knowing the oxide thickness before growing TiO_2 makes it easier to fit TiO_2 thickness after growth.

Tool: Woollam M-2000UI, Recipe: 8um oxide

A.2 TiO sputtering

Deposit TiO

Each TiO deposition is run for a maximum of 45 minutes. If thicker layers are necessary, repeat the 45 minute deposition until the desired layer thickness is reached. Between 45 minute depositions, the deposition rate can be monitored, by using ellipsometry to measure the thickness of the TiO_2 layer.

Tool: TCOater

Base pressure	1×10^{-6} mbar
Process pressure	6×10^{-3} mbar
Pre-sputter time	2 min
Temperature	20 °C
Rotation speed	5 RPM
Substrate height	44 mm
Reactor Ar flow	34 sccm
Reactor O ₂ flow	7.5 sccm
Gun Ar flow	0 sccm
Power	500 W

TiO₂ thickness measurement

To measure the thickness of the TiO₂ layer, the ellipsometer can be used again. The recipe 'TiO₂_on_8um_new' can be used for this. The oxide thickness measured before the start of the deposition should be entered into the model, otherwise it likely cannot find a good fit.

A.3 Photolithography

Dehydration

Tool: Hotplate, WB21

Temperature	120 °C
Time	5 min

HMDS Priming

Tool: Spinner, WB21

Primer	HMDS
Rotation speed	4000 RPM
Time	30 s

Photoresist spinning

Tool: Spinner, WB23

Resist	OlinOir 907-17
Rotation speed	4000 RPM
Time	30 s

Pre-exposure bake

Tool: Hotplate, WB21

Temperature	95 °C
Time	90 s

Anti sticking coating spinning**Tool: Spinner, WB20**

The AZ Aquatar is applied to the sample using a pipette. Clad spinner drain bath in aluminium foil before spinning, so cleanup is easy.

Coating	AZ Aquatar
Rotation speed	2500 RPM
Time	30 s

Exposure**Tool: Maskaligner EVG620**

Don't forget to apply sealing ring for vacuum contact around the wafer holder before loading the wafer.

Exposure time	3.8 s
Contact	Vacuum contact, at least -700 mbar

Post-exposure bake**Tool: Hotplate, WB22**

Post exposure bake is done at 110 °C instead of the standard 120 °C because the AZ-Aquatar cannot handle 120 °C.

Temperature	110 °C
Time	1 min

Development**Tool: OPD4262 beakers, WB21**

OPD4262 beaker 1	25 s, agitate constantly
OPD4262 beaker 2	25 s, agitate constantly
Quick dump rinser	Until a conductivity of $10 \text{ M}\Omega \text{ cm}^{-1}$ is reached
Dry spinner	2500 rpm for 75 s, with a 45 s N ₂ purge

Hardbake**Tool: Hotplate, WB22**

Post hardbake is done at 110 °C instead of the standard 120 °C because the AZ-Aquatar cannot handle 120 °C.

Temperature	110 °C
Time	30 min

A.4 Etching

RIE etching

Tool: Oxford PlasmaPro 100 Cobra

The settings are saved as a recipe, called 'TiO₂ etch modified ignite'. The expected etch rate for TiO₂ is 81 ± 4 nm/min.

Pressure	10 mTorr
O ₂ flow	6 sccm
Ar flow	5 sccm
SF ₆ flow	25 sccm
ICP Power	1500 W
HF Power	20 W
Temperature	10 °C

Resist stripping

Tool: Beaker with Microstrip 5010 on hotplate in WB01

Microstrip is not in a pre-filled beaker, therefore, the beaker will have to be filled manually.

Solution	Microstrip 5010
Temperature	85 °C
Time	10 min

The wafer is then cleaned and dried in the following way:

Quick dump rinser	Until a conductivity of $10 \text{ M}\Omega \text{ cm}^{-1}$ is reached
Dry spinner	2500 rpm for 75 s, with a 45 s N ₂ purge

Appendix B

Determining propagation losses from images using Matlab

The code used to extract propagation losses from images of waveguides with light coupled in is given below, with comments given for each major step, and all inputs. It depends on 2 pixel values given by the user, and 2 real dimensions of the waveguides. The code assumes the spirals rotate clockwise inwards.

B.1 Matlab code

```
1 %% Initialize special points
  % your inputs
3 image = ; % Source image in greyscale
  parm.O = []; % Pixel [x y] of spiral center
5 parm.S = []; % Pixel [x y] of starting point of fit
  parm.Pp = ; % Spiral pitch in pixels
7 parm.Pu = ; % Spiral pitch in microns
  parm.D_start = ; % Initial radius in microns ( at point S)
9 noOfSamples = 400; % Amount of datapoints for fit
  angleToSweep = 270; % Angle along spiral swept by datapoints
11 startAngle = 0; % Angle to sweep without taking datapoints. Can be used to
    % Exclude saturated pixels near start of spiral
13 baseLine = ; % Background intensity

15 % calculated inputs
  s = parm.S-parm.O; % transform s to coordinate system around spiral center
17 parm.theta_s = atan(s(2)/s(1)); % calculate angle of init. point to origin
  parm.D_s = sqrt(s(1)^2+s(2)^2); % calculate distance from origin in pixels
19
  %% Filter image with circular filter , to make ring easier to hit
21 H = fspecial('disk', 5);
  filteredImage = imfilter(image, H);
23 figure();
  imshow(filteredImage);
25 hold on;
```



```

scatter(parm.O(1), parm.O(2)); % plot origin in image to check
27
%% Generate datapoints, and get their intensities
29 thetas = linspace(startAngle, startAngle+angleToSweep, noOfSamples); %
                                     % angles where datapoints are taken
31 distances = deg2distance(thetas, parm); %
                                     % distance propagated for each datapoint, in microns
33 distances = distances * 1e-4; % now in centimeters
intensities = zeros(1,noOfSamples);
35
samplePoints = deg2point(thetas', parm);
37 samplePoints = round(samplePoints);

39 scatter(samplePoints(:,1), samplePoints(:,2)); % plot samples on image
for i=1:noOfSamples % loop over sample angles, and get intensities
41     intensities(i) = filteredImage(samplePoints(i,2),samplePoints(i,1));
end
43 intensities = intensities-baseLine; % subtract background signal

45 %% Plot and fit intensity vs distance
figure();
47 hold on;
% fitting code
49 [xData, yData] = prepareCurveData( distances, intensities );
% Set up fittype and options.
51 ft = fittype( 'exp1' ); % exp1 = single exponential
opts = fitoptions( 'Method', 'NonlinearLeastSquares' );
53 opts.Display = 'Off';
opts.Robust = 'Bisquare';
55 [fitresult, gof] = fit( xData, yData, ft, opts ); % fitresult delivers
                                     % -alpha in cm-1
57
%% plot fitresult on top of datapoints
59 %plot(fitresult, 'k');
plot(fitresult,distances,intensities%,toDrop)
61 dBcm = -fitresult.b*4.34; % convert to dB/cm
%xlim([0 0.6]);
63 legend('datapoints', string(dBcm)+' dB/cm fit');
xlabel('Propagation distance (cm)');
65 ylabel('Intensity (a.u.)');
title('Light intensity along waveguide');
67 confInterval = confint(fitresult);
confInterval = confInterval(:,2)*-4.34; % confidence interval in dB/cm
69
%% print linear results
71 disp(filename)
disp(dBcm)
73 disp(confInterval)

75 %% function declarations
function point = deg2point(theta_in, parm)
77 % takes an angle from starting point, and returns the point in X,Y
% coordinates where it is in image. Therefore, 540 degrees is not the same

```

```

79 % as 180, since it will be 1 ring closer to the center
D_new = parm.D_s - parm.Pp.*(theta_in./360);
81 theta_new = parm.theta_s + ((theta_in./360).*(2*pi));
[xpix,ypix] = pol2cart(theta_new,D_new);
83 xpix = xpix + parm.O(1);
ypix = ypix + parm.O(2);
85 point = [xpix ypix];
end

87
function D = deg2distance(theta_in, parm)
89 % converts number of degrees travelled from initial point into actual distance
% travelled from first point, using already solved line integral
91 D=(pi/180).*theta_in.*parm.D_start-(pi/180).*parm.Pu.*(theta_in.^2)./(720);
end

93
function I = point2I(point, image, H)
95 I = image(round(point(2)), round(point(1)));
% Necessary to return NaN if the requested point is outside of image,
97 % otherwise requested index does not exist
%if(point(1) > 2 && point(1) < 254 && point(2) > 2 && point(2) < 318)
99 %    I = image(round(point(2)), round(point(1)));
%else
101 %    I = NaN;
%end
103 end

```


Appendix C

XPS measurements

The slides received with the CPS measurement results are printed below.

UNIVERSITY OF TWENTE.

MESA+ INSTITUTE FOR NANOTECHNOLOGY



XPS measurements report for Ewoud Vissers, OS

UNIVERSITEIT TWENTE. KIPXPS180726001 **MESA+**

Goal of the XPS measurements

Problem description: A wave guide made of TiO₂ shows too much absorption for the wavelength used. Measurements give a hint for the presence of OH groups in the material. Can XPS help to clarify the problem?

Investigations:

- Survey scans are made to see the gross overall atomic content of the surface layer. All elements except H and He can be visible. From B up to U, with concentrations as low as 1%. Pollutants can show up and sometimes explained by the researcher.
- Element spectra scans are made with a better energy resolution and lower noise than the survey spectra. The atomic concentrations of the elements measured can be calculated and chemical shifts will show up for certain compound materials. The atomic concentration is calculated with the formula $Cx = \frac{I_x/S_x}{\sum_i I_i/S_i}$ with I_i the peak area of a photoelectron peak and S_i the relative sensitivity factor of the peak.
- Depth profiles are generated to see how contents can change with depth. Thin film thicknesses can be measured if the sputter rates are known with respect to silicon oxide.

UNIVERSITEIT TWENTE.

KIPXPS180726001

MESA+

Instruments and conditions

- Date : July 26, 2018
- Location : Materials Characterisation at Nanolab at the University of Twente
- Machine : Quanterra SXM (scanning XPS microprobe) from Physical Electronics
- Operator : Gerard Kip
- X-ray : Al K α , monochromatic at 1486.6 eV
- Manual check of the X-ray beam:
 - I_0 : 2.6 mA
 - Power : 50 W
 - Beam size : 200 μ m (mappings are often done with beam sizes down to 9 μ m)
- Pressure
 - Base pressure : < 1 e-9 torr, no problems with vacuum
 - Working pressure : ~ 3 e-8 torr. The greatest part is argon for neutralization
- Neutralizers on auto if the samples are non conducting.
 - Low energy electron flood gun is used to supply the missing photo- and Auger electrons
 - Low energy Argon ions are used to remove the surplus of electrons put there by the electron flood gun
 - The result is a very stable potential at the acquisition area. The potential is close to, but not exactly, 0 V. Reference elements, mostly carbon, are used to calibrate the energy scale
- Auto-Z height : 24.10 mm and up, depending on platen position, done with the 5 μ 1.25W15keV X-ray beam at the standard beam-input and detector input angle of 45°. Auto-Z is necessary for alignment of the surface of the sample with the foci of X-ray source and electron analyzer
- Software: Compass for XPS control, Multipak v.9.8.0.19 for data reduction. Fitting of spectra is mostly done after shifting of the measured spectra with respect to known reference binding energies. Aliphatic carbon C1s at 284.8 eV or gold Au4f7/2 at 83.96 eV, silver Ag3d5/2 at 368.21eV and copper Cu2p3/2 at 932.62 eV
- Sample Material State Point/Area/Linescan/Mapping

1 360 nm TiO ₂ on SiO ₂	Solid	areas chosen for acquisitions
2 80 nm TiO ₂ on Si		

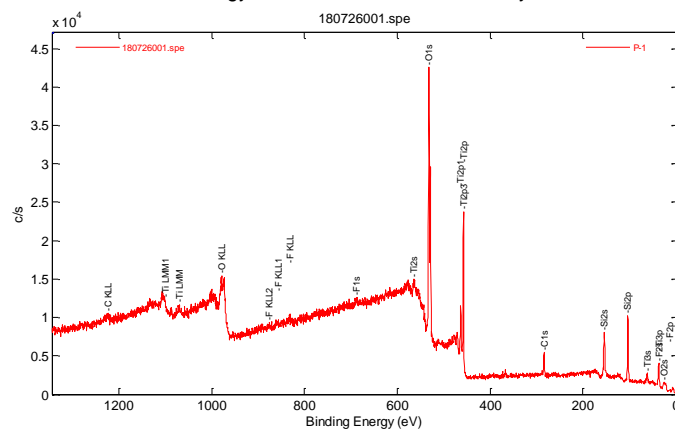
UNIVERSITEIT TWENTE.

KIPXPS180726001

MESA+

Sample 1

Survey spectra, from -5 eV - 1345 eV.
Pass Energy = 224eV and $\delta E=0.4\text{eV}$. 3 cycles

Atomic Concentration Table

Area	C1s	O1s	F1s	Si2p	Ar2p	Ti2p	
	0.314	0.733	1.000	0.368	1.231	2.077	RSF
	70.102	163.846	223.669	95.494	308.385	509.717	CorrectedRSF
P-1	8.79	63.10	1.44	17.38	0.00	9.29	

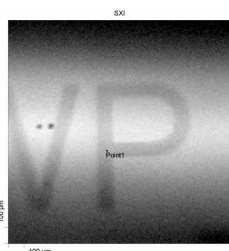
UNIVERSITEIT TWENTE.

KIPXPS180726001

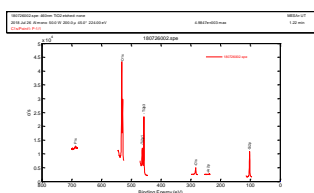
MESA+

Sample 1

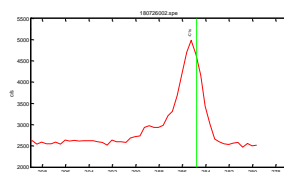
Element spectra scans on C, O, F, Si, Ar and Ti



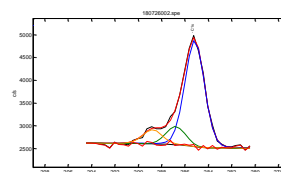
Acquisition points



C1s spectra as measured



C1s fit after shift of the main C1s band to 284.8 eV, the reference.



Spec	Band	Pos	PosSep	B_FWHM	FWHM	Height	%Gauss	Area	%Area	ChiSquared
1	1	285.17	0.00	1.94	1.94	2334	92	5004	76.57	1.24
2	2	286.80	1.63	1.94	1.94	401	100	829	12.69	
3	3	288.77	3.60	1.94	1.94	314	83	702	10.74	

Atomic Concentration Table

AreaComment	C1s	O1s	F1s	Si2p	Ar2p	Ti2p	
	0.314	0.733	1.000	0.368	1.231	2.077	RSF
	70.102	163.846	223.669	95.494	308.385	509.717	CorrectedRSF
P-1	8.06	62.21	1.47	18.50	0.00	9.76	

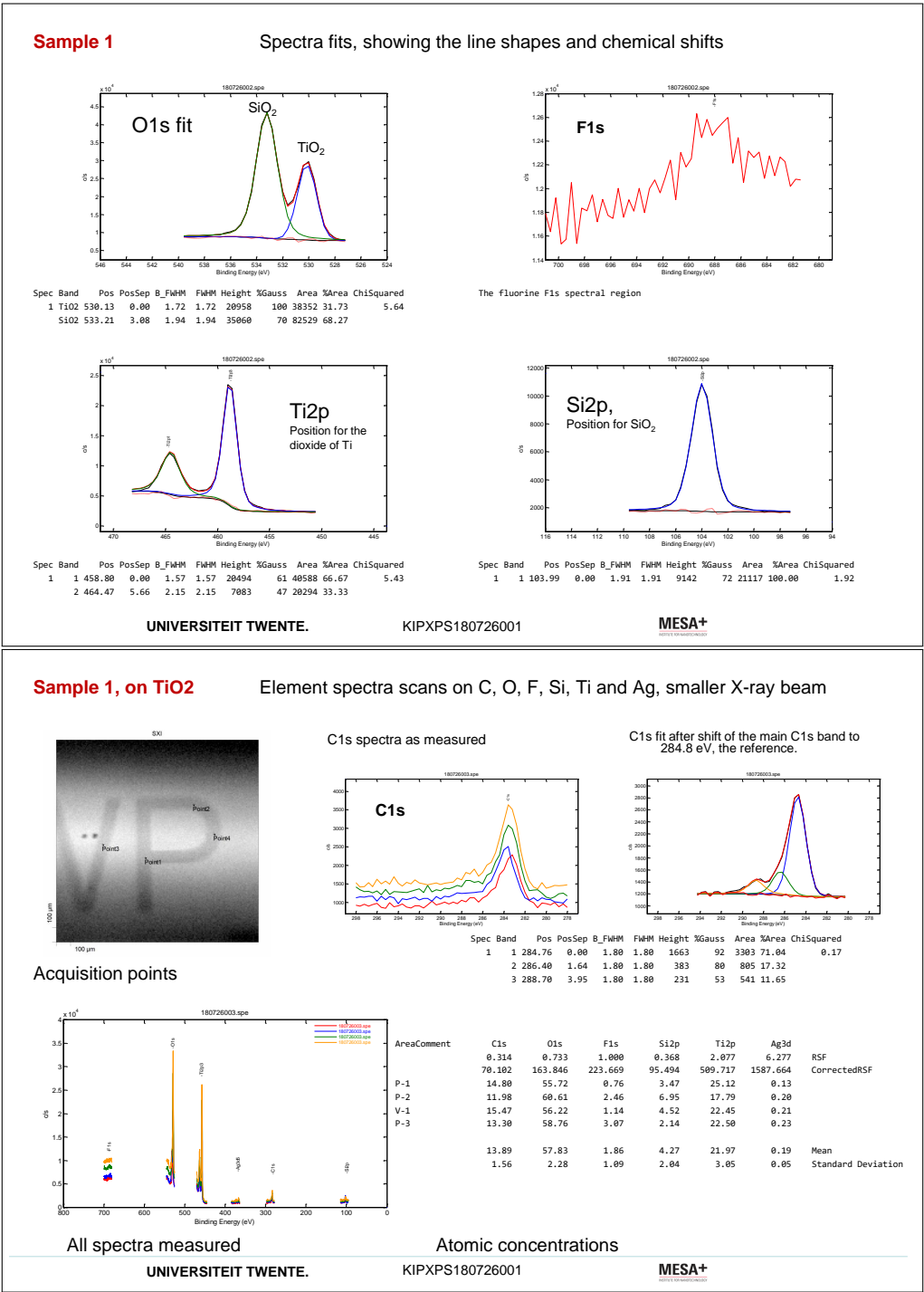
All spectra measured

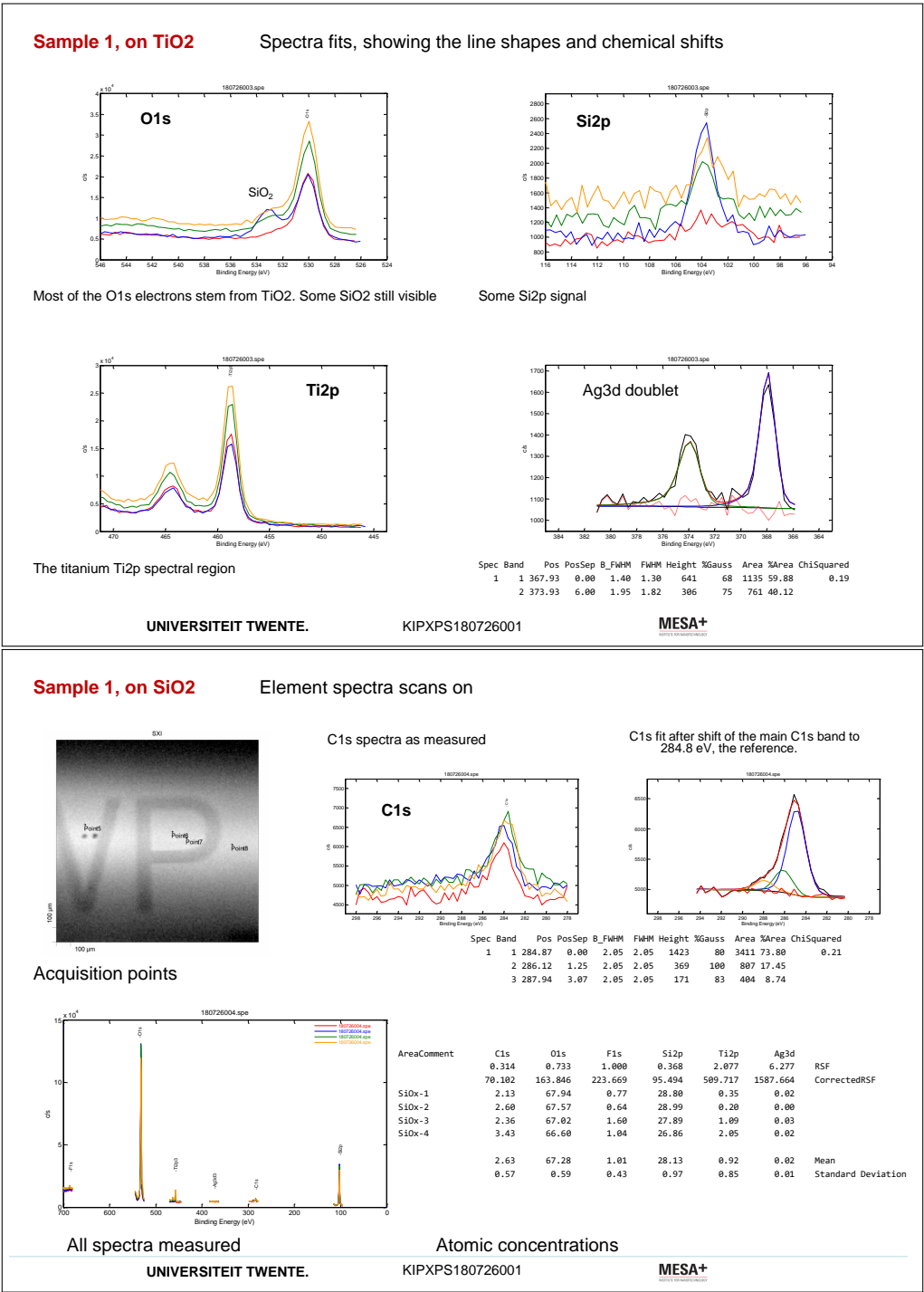
Atomic concentrations

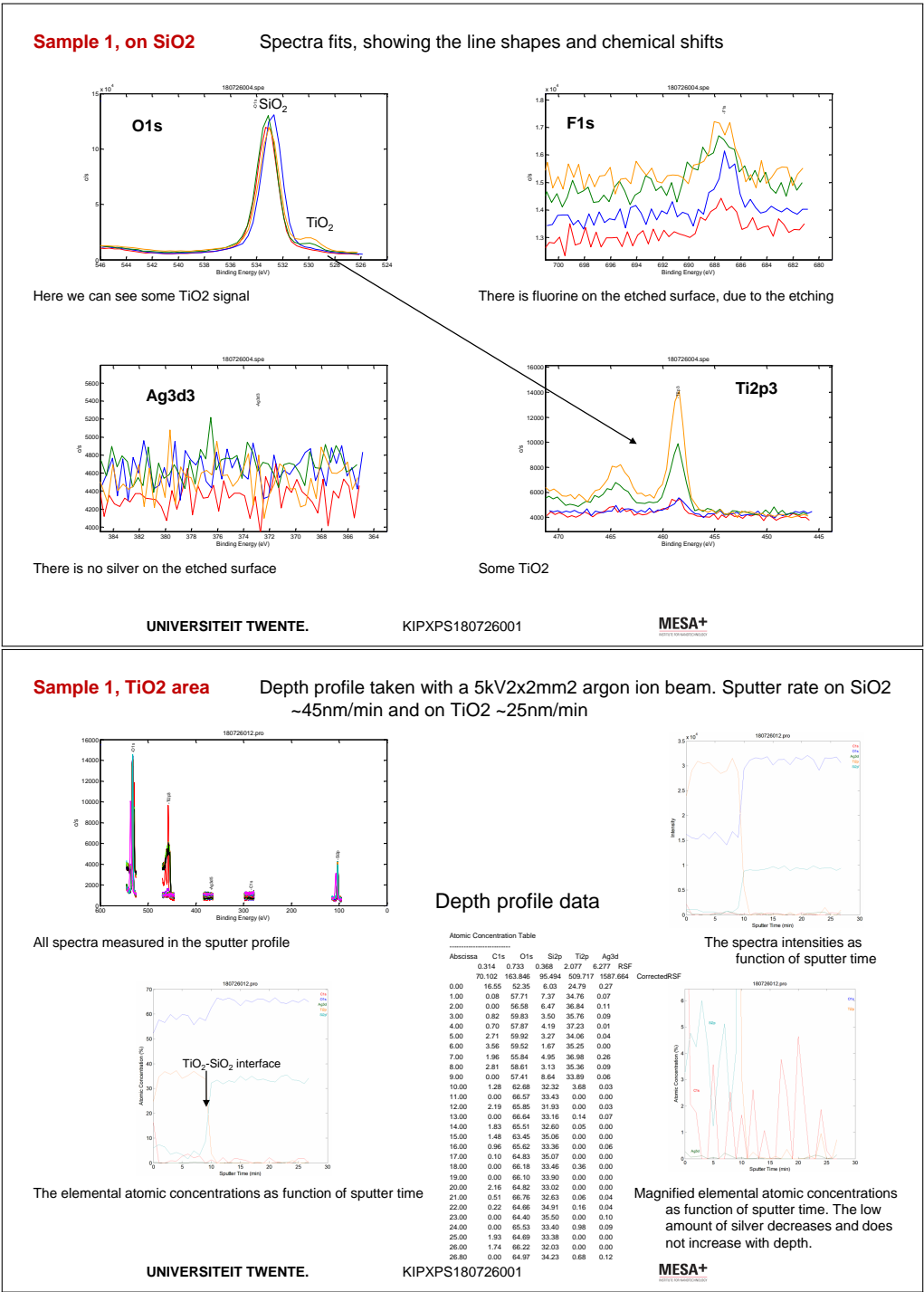
UNIVERSITEIT TWENTE.

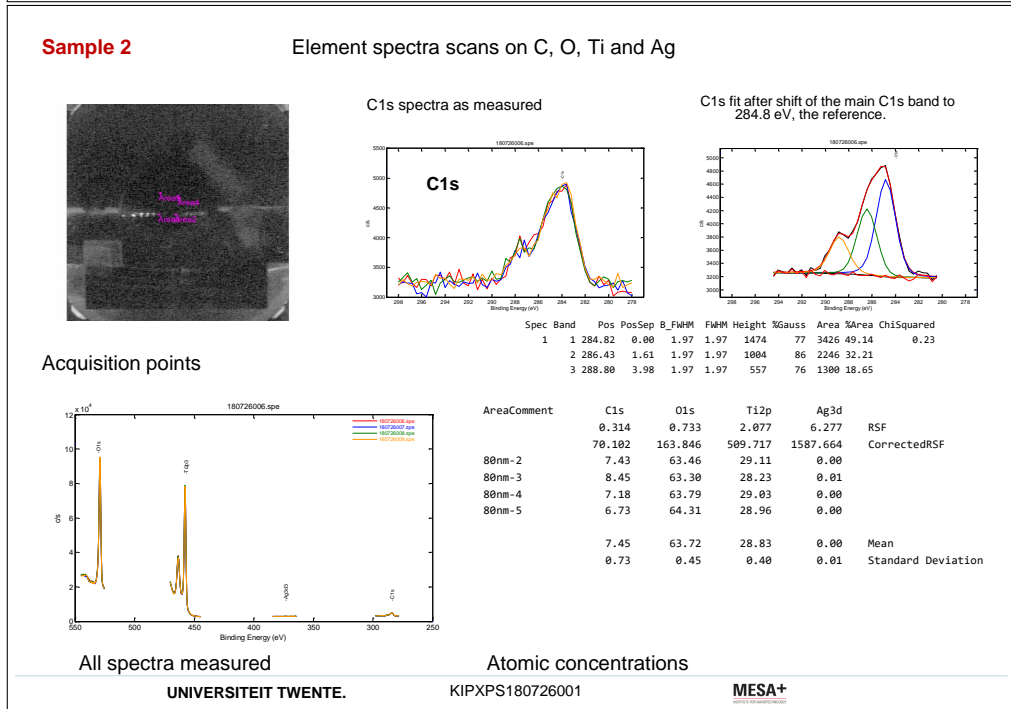
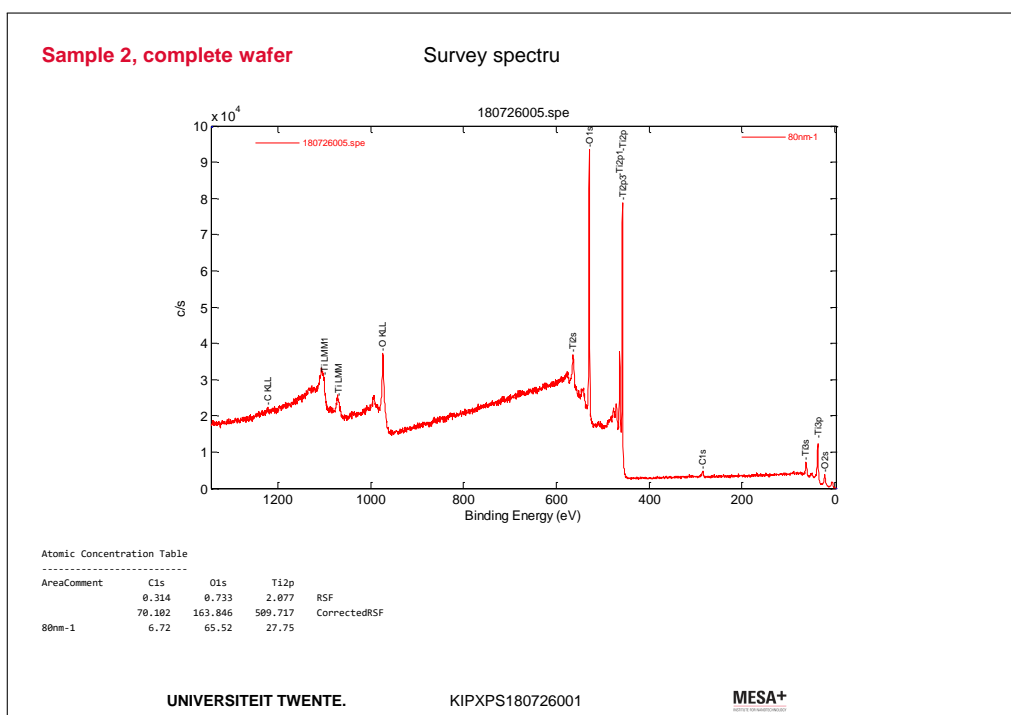
KIPXPS180726001

MESA+



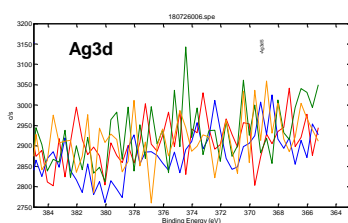
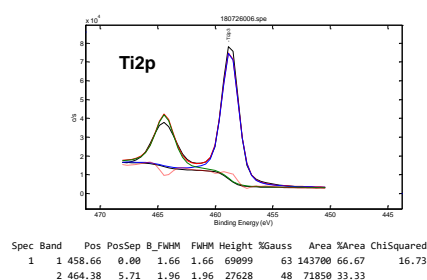
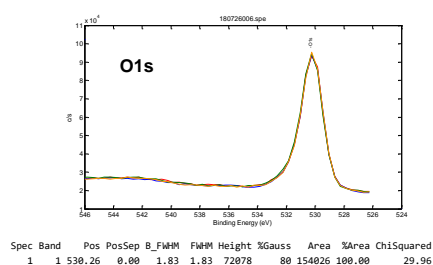






Sample 2

Spectra fits, showing the line shapes and chemical shifts



No silver spectrum is visible. So silver is not made on this wafer

UNIVERSITEIT TWENTE.

KIPXPS180726001

MESA+

Remarks on KIPXPS18072601**Ewoud Vissers****Optical Systems**

- Two samples were measured with XPS.
- On sample 1 we choose acquisition points on the free etched TiO₂ parts of the wave guide system. The survey scan indicated the presence of the elements carbon, oxygen, fluorine, silicon, argon and titanium. Carbon is a standard contaminations on samples that have been in ambient air for a while. The fluorine can be due to the etching proces. The silicon comes from the fact that the X-ray beam diameter is chosen as wide as the TiO₂ structures. The sides of the Gaussian X-ray beam produces these Si electrons. Oxygen and titanium should be there. The peak at 465 eV (firts wrongly given to Ar) should not be there, unless Ar is implanted during etching.
- Core spectra scans indicate that 1: the chosen beam energy (width of the beam) was to high. 2: with smaller beam size the Si signal disappears as well as one of the oxygen peaks and that argon was a misinterpretation that should be silver. Silver is definitely present at the surface of the TiO₂ structures.
- The spectra taken on the whole wafer does not show any silver. The TiO₂ was made at another time than the etched wafer.
- Contrary to what I expected does the depth profile not show much silver. I expected the silver signal to increase with depth if it would be deposited by the process in the T-coater. This did not happen. The silver is on the etched TiO₂ surface only and not in the layer itself.

Time spent [hours]

OFI no.	: ???
Sample preparation and mounting	: 0.5
XPS point / area selection including focusing	: 0.2
Survey spectra scans	: 0.5
Element spectra scans	: 1.8
Depth profiles / AR-XPS / Mappings	: P.M.
Data reduction	: 0.75
Report writing	: 0.75
Consultation	:

UNIVERSITEIT TWENTE.

KIPXPS180726001

MESA+

References

- **Standard books used for interpretation of spectra:**
 - Handbook of X-ray Photoelectron Spectroscopy
 - J. F. Moulder, W. F. Stickle, P. E. Sobol, K. D. Bomben, *Handbook of X-ray Photoelectron Spectroscopy*, Perkin-Elmer Corporation, Eden Prairie (1992)
 - High Resolution XPS of Organic Polymers
 - G. Beamson and D. Briggs, *High Resolution XPS of Organic Polymers: The Scienta ESCA300 Database*, John Wiley & Sons, Chichester (1992)
 - Handbook of X-ray Photoelectron Spectroscopy
 - N. Ikeo, Y. Iijima, N. Niimura, M. Sigematsu, T. Tazawa, S. Matsumoto, K. Kojima, Y. Nagasawa, *Handbook of X-ray Photoelectron Spectroscopy*, JEOL (1991)
 - High Resolution XPS Spectra of Polymers
 - K. Robinson, *High Resolution XPS Spectra of Polymers*, Kratos Analytical (1992)
- **Software used**
 - PHI Multipak V9.8.0.19., 2017-03-23, Copyright © Ulvac-phi Inc., 1994-2017
 - CasaXPS VAMAS Processing Software V2.3.14, Copyright © Neal Fairley, 1999-2008
 - NIST Database for the Simulation of Electron Spectra for Surface Analysis - Version 1-1, W.S.M. Werner, W. Smekal and C.J. Powell, National Institute of Standards and Technology, Gaithersburg, MD (2006)
- **Extra information used**
 - NIST X-ray Photoelectron Spectroscopy Database 20, Version 4.1 (Web Version), Data compiled and evaluated by Alexander V. Naumkin, Anna Kraut-Vass, Stephen W. Gaarenstroom, and Cedric J. Powell
Standard Reference Data Group
National Institute of Standards and Technology, Gaithersburg, (2003);
<http://srdata.nist.gov/xps>
 - Practical Surface Analysis (Second Edition) Volume 1: Auger and X-ray Photoelectron Spectroscopy, Edited by D.Briggs and M.P. Seah, © 1990 John Wiley & Sons Ltd
 - An informative database from Thermo
<http://xpsimplified.com/periodictable/>
 - LaSurface database sponsored by Thermo Electronics
<http://www.Lasurface.com>